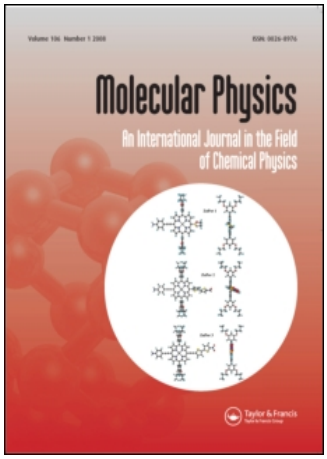

Molecular Physics
An International Journal in the Field of Chemical Physics
Publication details, including instructions for authors and subscription information:
http://www.informaworld.com/smpp/title~content=t713395160

First-principles-derived kinetics of the reactions involved in low-temperature dimethyl ether oxidation

Amity Andersen; Emily A. Carter [a]
[a] Department of Mechanical and Aerospace Engineering and Program in Applied and Computational Mathematics, Princeton University, Princeton, NJ 08544-5263, USA

Online Publication Date: 01 January 2008
To cite this Article: Andersen, Amity and Carter, Emily A. (2008) 'First-principles-derived kinetics of the reactions involved in low-temperature dimethyl ether oxidation', Molecular Physics, 106:2, 367 - 396
To link to this article: DOI: 10.1080/00268970701837008
URL: http://dx.doi.org/10.1080/00268970701837008

Molecular Physics
Vol. 106, Nos. 2–4, 2008, 367–396

RESEARCH ARTICLE

First-principles-derived kinetics of the reactions involved in low-temperature dimethyl ether oxidation

Amity Andersen[a] and Emily A. Carter[b]*

[a]*Accelrys, Inc., 10188 Telesis Court, Suite 100, San Diego, CA 92121, USA;* [b]*Department of Mechanical and Aerospace Engineering and Program in Applied and Computational Mathematics, Princeton University, Princeton, NJ 08544-5263, USA*

(*Received 18 October 2007; final version received 29 November 2007*)

Spin-polarised density functional theory (DFT-B3LYP) energies, harmonic vibrational frequencies, and moments of inertia are used to construct modified Arrhenius rate expressions for elementary steps in chain-propagation and chain-branching pathways for dimethyl ether combustion. Barrierless reactions were treated with variational RRKM theory, and global kinetics were modeled using master equation and perfectly stirred reactor simulations. Our kinetics analysis suggests that the bottleneck along the chain propagation path is the isomerisation of CH_3OCH_2OO, contrary to earlier interpretations. Comparing the rate constants for competing decomposition pathways of the key chain-branching intermediate hydroperoxymethyl formate (HPMF), we find that formation of formic acid and the atmospherically relevant Criegee intermediate (CH_2OO) via a H-bonded adduct may be more favourable than O–O bond scission. Since the latter forms a source of a second OH radical beyond that supplied in chain propagation, which is necessary for explosive combustion, the more favourable pathway to formic acid may inhibit autoignition of the fuel. We predict that the HPMF O–O scission product, $OCH_2OC(=O)H$, most likely directly dissociates to $HCO + HC(=O)OH$. This implies an overabundance of CO at 550–700 K, since $HC(=O)OH$ is a fairly stable product in this temperature range and facile H abstraction from HCO leads to CO. We find that CO_2 product yields are sensitive to the creation of CH_2OO and that creation of CH_2OO is competitive with the O–O scission reaction.

Keywords: combustion; kinetics; dimethyl ether; oxidation; density functional theory

1. Introduction

Dimethyl ether (DME) has been proposed as an alternative diesel fuel. Its propensity to autoignite under diesel conditions is comparable to that of conventional diesel (having about the same cetane number >55). Unlike conventional diesel (which is composed of long-chain hydrocarbons), dimethyl ether combustion is virtually soot-free. Dimethyl ether has other appealing properties such as its low toxicity and low photo-reactivity. It may also be produced cheaply via a one-step synthesis process and stored in the presently available liquid petroleum gas (LPG) infrastructure [1].

It is the motivation of this study and our past investigations [2,3] to shed light on the underlying mechanism responsible for dimethyl ether's low-temperature autoignition. Though some general experimental observations and measurements are available for dimethyl ether combustion (such as some kinetics data and some information about the products), our previous studies have called into question the completeness of the latest available mechanism [4,5] for the low-temperature oxidation of DME. Thus it is our intention here to try to understand key aspects of the low-temperature autoignition by looking at trends in the kinetics within an augmented mechanism.

In low-temperature autoignition of analogous alkane systems, low-temperature kinetics is thought to occur via a chain-branching mechanism. In the case of dimethyl ether, the initiation reaction occurs when a hydrogen is abstracted from dimethyl ether by a reactive species such as O_2, ·OH, or HOO· (with ·OH being the most reactive). Following the abstraction of a hydrogen atom, the resulting $CH_3O\dot{C}H_2$ radical combines with O_2 to form a $CH_3OCH_2OO\cdot$ radical. This radical can undergo a series of reactions to eventually form two formaldehyde molecules and a ·OH. This ·OH can then 'propagate' a chain reaction by attacking another DME molecule. Alternatively, $CH_3OCH_2OO\cdot$ can isomerise to form a $\cdot CH_2OCH_2OOH$ radical, which can combine with an O_2 to form $\cdot OOCH_2OCH_2OOH$. This highly

*Corresponding author. Email: eac@princeton.edu

ISSN 0026–8976 print/ISSN 1362–3028 online

DOI: 10.1080/00268970701837008
http://www.informaworld.com

oxygenated radical then has the potential to undergo a round of reactions that can form two ·OH radicals instead of one (as in chain propagation). This leads to branched chain reactions which cause an exponential increase in the rate of dimethyl ether oxidation. Details of the individual mechanistic steps will be discussed later on.

Experimental information on the kinetics of low-temperature dimethyl ether combustion is very sparse. Many experimental studies focus on aspects of dimethyl ether combustion that are easily controlled (pressures of 1 atm or less and at 298 K), such as the studies done by Sehested *et al.* [6,7], but are not very relevant to the high temperatures and high pressures attained in diesel engines. Some experimental studies focus more on qualitative trends in the appearance of stable products (e.g., Liu *et al.* [8]). However, the most complete experimental/modelling studies to date are those done by Curran and coworkers [4,5,9]. We will focus primarily on the mechanism proposed by Curran and coworkers, along with issues concerning the chain-branching mechanism that we have brought forth in our previous work [3].

In Curran *et al.*'s kinetics models, many of the rate expressions of elementary reactions involved in the low-temperature combustion of dimethyl ether have been estimated with empirical methods. Yamada *et al.* [10] have calculated the potential energy surface of the chain propagation mechanism using the CBS-q electronic structure method with MP2-optimised geometries. We have found discrepancies between our calculations and those of Yamada *et al.* in our past work [2], and will be revisiting these on the kinetics front. On the other hand, the species involved in chain-branching have never (to the best of our knowledge) been studied with electronic structure methods until our recent work [3]. These results will also be used to derive knowledge of the kinetics dominating low-temperature combustion. In particular, we will look at hydroperoxymethyl formate (HPMF) decomposition, which may lead to Criegee intermediate formation, a proposed key intermediate in ozonolysis of alkenes. Here we will look at the kinetics implications of the rate expressions derived from the first-principles data from our past work [2,3] and the present work.

2. Theoretical methods

2.1. *Electronic structure calculations*

In our previous work [2,3], we calculated energies, optimised molecular structures, and harmonic vibrational frequencies at the spin-polarised (U) DFT-B3LYP [11]//6-311G** [12] level of theory. As in previous studies [2,3], we emphasise here that DFT-B3LYP gives a comparable description of the $CH_3\dot{C}H_2 + O_2$ (an analogous system) potential energy surface to recent CCSD(T) calculations of Rienstra-Kiracofe *et al.* [13] DFT-B3LYP also gives a good description of the potential energy surface of carbonyl oxide (CH_2OO) reactions. [14–16] Use of 'higher' level energetics calculations (e.g., G2 and CBS-Q) was not considered here because of the size of the largest species we investigate (seven centers, five of which are oxygens). Thus, for consistency, all optimised structures were calculated at the DFT-B3LYP//6-311G** level of theory. The estimated average error of DFT-B3LYP energies is $\sim$3–4 kcal mol^{-1} [17,18]. Additional reactions pertaining to Criegee intermediate reactions have been introduced into the present work. Thus, additional electronic structure calculations to find appropriate total energies, local minima and transition state geometries, and harmonic vibrational frequencies were necessary. Where applicable, energetics for these additional reactions will be briefly addressed in Section 3.

2.2. *Rate constant calculations for unimolecular and recombination reactions*

2.2.1. *Calculation of phenomenological rate constants*

Conventional transition state theory (CTST) as implemented in KHIMERA [19,20] was used to calculate the rate constants of all reactions considered in this study. In CTST, the rate constant as a function of temperature is calculated using the following equation:

$$k(T) = \frac{k_B T}{h}\frac{Q^{\ddagger}}{Q}\exp\left(-\frac{\Delta E_0}{k_B T}\right), \qquad (1)$$

where k_B is the Boltzmann constant, T is the temperature, h is Planck's constant, ΔE_0 is the zero-point-corrected energy difference between the activated complex (transition state) and the reactant, and $Q^{\ddagger}$ and Q are the total partition functions for the activated complex and the reactant, respectively (note that for a bimolecular reaction Q is represented by a product of two total partition functions, $Q_A Q_B$). The total partition function is a product of the translational, vibrational, rotational, and electronic partition functions. Thus, to calculate the total partition function for a given species, knowledge of the harmonic vibrational frequencies, moments of inertia, and electronic states are needed and have been calculated here using DFT-B3LYP.

For unimolecular and recombination reactions, CTST gives an estimation of the rate constant in the high-pressure limit (k_∞). Since diesel engines operate with pressure conditions ranging from 1 to 90 atm (finite pressure), it is important to check if the unimolecular or recombination reaction rate constant at a given temperature is close to or smaller than the high-pressure limit rate constant. This is done by calculating unimolecular and recombination rate constants with RRKM theory [21–23]

$$k(E) = \left(\frac{m^{\ddagger}\sigma g_e^{\ddagger}}{m\sigma^{\ddagger} g_e}\right)\frac{N^{\ddagger}(E-E_0)}{h\rho(E)}, \qquad (2)$$

where the rate constant k is written as a function of energy (microcanonical), $m^{\ddagger}$ and m are the number of optical isomers, $\sigma^{\ddagger}$ and σ are the external symmetry numbers, $g_e^{\ddagger}$ and g_e are the electronic degeneracies of the transition state and the reactant, respectively, $N^{\ddagger}(E-E_0)$ is the sum of ro-vibrational states of the transition state (i.e. the total number of states with energy $\leq E-E_0$), $\rho(E)$ is the density of ro-vibrational states of the reactant, and E_0 is the threshold energy for reaction. Recombination (e.g., $A+B \rightarrow AB$) rate constants are calculated from the corresponding reverse unimolecular decomposition (e.g., $AB \rightarrow A+B$) reaction using detailed balance (i.e. $k_r = k_d/K_{eq}$ where k_r is the recombination rate constant, k_d is the decomposition rate constant and K_{eq} is the equilibrium constant) [22]. Typically, unimolecular rate constants approach the high-pressure limit around 1 atm at 298 K. However, convergence to the asymptotic high-pressure limit may be more gradual as the temperature is increased [22]. Steady-state master equation RRKM rate constants (Equation (2)) were calculated using KHIMERA [19,20]. The collision model for downward energy transfer used for master equation calculations is the exponential-down model

$$P_d(E,E') = \frac{1}{N(E')}\exp\left(\left|\frac{E'-E}{\alpha}\right|\right) \quad (E'>E), \qquad (3)$$

where $P_d(E,E')$ is the probability of downward (deactivating) collisional energy transfer from internal energy E' to E, $N(E')$ is a normalisation factor, and α is a constant equivalent to the average transfer energy of a deactivating collision $\langle\Delta E\rangle_d$ at moderate-to-high energies [22,24]. N_2 was chosen as the bath gas (majority species in air) and $\langle\Delta E\rangle_d$ was set to 500 cm^{-1}. This value is almost half way between a weak inert gas collider ($\sim$100 cm^{-1}) and a strong collider ($\sim$1000 cm^{-1} or greater) and is sufficient for most practical applications [19,22,24]. For more information concerning the theory and implementation of KHIMERA, see Novoselov *et al.* [19].

The temperature dependence of a reaction rate constant for a desired temperature range can be expressed with a modified Arrhenius nonlinear fit of the rate constant

$$k(T) = AT^n \exp(-E_a/RT), \qquad (4)$$

where A is the pre-exponential factor, T is the temperature, n is a parameter describing the temperature dependence of the pre-exponential factor, E_a is the activation energy, and R is the ideal gas constant. For a given reaction, the rate constant is fitted using Equation (4) over a specified temperature range. Reaction rate constants were fitted over a temperature range of 298–2000 K at the high-pressure limit (CTST calculated rate constants) and pressures of 1, 10, and 40 atm (RRKM/master equation calculated rate constants). These expressions of 'phenomenological' rate constants can then be used as mechanistic input to model global kinetics in programs such as CHEMKIN [25].

The transition states for reactions considered here fall under two categories: tight or loose. Reactions with tight transition states (those with a well-defined saddle-point structure) could be treated simply with harmonic oscillator/rigid-rotor RRKM calculations as implemented in KHIMERA [19,20]. The low-temperature dimethyl ether oxidation mechanism also involves simple scission reactions (radical–radical dissociation/recombination) where a saddle-point structure cannot be located using standard electronic structure packages. KHIMERA constructs a loose transition state based on the Gorin model [21–23], in which the constituent fragments are allowed to freely rotate (interacting via a Lennard–Jones potential) and their rotational degrees of freedom are included in the vibrational and rotational density of states integration [21,23]. This 'quasi-transition' complex is constructed from the DFT-B3LYP data for the reactants [19]. However, this method employed by KHIMERA does not variationally determine the distance between fragments as a function of temperature.

2.2.2. *Variational transition state theory rate constant calculations involving reactions with 'loose' transition states*

For a more accurate treatment of loose transition states involving a clear bond-breaking/formation process, we calculated rate expressions using the VARIFLEX code, which employs canonical and microcanonical variational transition state theories [26]. Lennard–Jones parameters for the species considered here were estimated from critical temperatures (T_c), pressures (P_c), and volumes (V_c) using methods

described in the compilation of Reid *et al.* [27] T_c, P_c, and V_c were estimated from the structures of stable species as implemented in ChemDraw [28]. For the loose transition state involving a clear bond-breaking/formation process, a potential energy surface of the pertinent bond breaking was constructed using DFT-B3LYP//6-311G**. Those reactions considered for this treatment will be specified in Section 3. The potential was fitted to a Varshni potential

$$V_{\text{Varshni}} = D_{e,A-B}\left(1 - \frac{r_{e,A-B}}{r_{A-B}}\exp[-\beta(r_{A-B}^2 - r_{e,A-B}^2)]\right)^2 - D_{e,A-B}, \quad (5)$$

where $D_{e,A-B}$ is the potential depth, β is a parameter, r_{A-B} is the variable bond distance between the bonding atoms of fragment A and fragment B, and $r_{e,A-B}$ is the equilibrium bond distance of the complex (AB) [29,30].

Microcanonical variational RRKM rates were calculated at the E/J-resolved level. Pressure-dependent rate expressions (1, 10, and 40 atm) were calculated by one-dimensional steady-state master equations solved with a matrix inversion based method [22,23]. The J distribution is represented by the Boltzmann probability of the complex (AB). The energy grain ('bin') size was chosen to be $100\,\text{cm}^{-1}$. The energy range was $-5000\,\text{cm}^{-1}$ (below the energy threshold, E_0) to $65{,}100\,\text{cm}^{-1}$ (above the energy threshold) to guarantee convergence of the integration over energy. The angular momentum (J) range was from 1 to 341, in steps of 10. The temperature was varied from 298 to 2000 K, and Equation (4) was used to fit the rate constant as a function of temperature.

2.3. *Time-dependent stochastic master equation simulations*

Time-dependent stochastic master equation simulations were performed using the Multiwell code [31,32]. Multiwell solves the time-dependent master equation stochastically rather than deterministically. Multiwell uses a hybrid formulation of the master equation. In this formulation, the low vibrational energy regime is treated with energy-graining (or 'binning'), and the high vibrational energy regime is treated as a quasicontinuum of states. For the systems considered here, an energy grain of $10\,\text{cm}^{-1}$ was selected, and 250 grains were allocated for the low vibrational energy regime. 250 'bins' were allocated for the high vibrational energy regime, and the energy range was set to 0–85,000 cm^{-1}. Thus the quasicontinuum regime was set to interpolate between points $341.4\,\text{cm}^{-1}$ apart. The intermediate and transition state species were treated as symmetric tops. The density of states for intermediate and transition state species were calculated from harmonic vibrational frequencies and moments of inertia calculated previously [2].

The collision model used in all simulations considered here is the exponential collision model of toluene $+O_2$ (bath gas), which has been studied experimentally by Toselli *et al.* [33]. In this case, the parametrisation of the α for the exponential collision model is a function of energy rather than a constant (as implied in Equation (3)). Thus, for toluene and O_2, it is $\alpha(E) = 35.4 + 0.0142E - 1.63 \times 10^{-7}E^2$ (where E is the energy). The Lennard–Jones parameters of O_2 from the Toselli *et al.* [33] study ($\epsilon/k_B = 71.4\,\text{K}$ and $\sigma = 3.48\,\text{Å}$) were used for the bath gas in the collision model. Lennard–Jones parameters for stable species were estimates from T_c, P_c, and V_c, as described in the previous section.

Initial internal energies for chemically activated (vibrationally excited) species are determined by Monte Carlo selection. Selection of internal energy is made over a specific number of stochastic trials. The selected time duration for these simulations was $5 \times 10^{-6}\,\text{s}$, and the number of stochastic trials was 10,000. Microcanonical rates for individual unimolecular reactions are calculated automatically by Multiwell via RRKM theory for evaluation of the master equation. For unimolecular reactions with an apparently 'barrierless' transition state, the inverse Laplace transform method [21], as implemented in Multiwell, was used to derive microcanonical rates from an estimate of A_∞. Further system-dependent details will be discussed in the results section.

2.4. *Global kinetics simulation in a perfectly stirred reactor*

The reaction mechanism developed by Fischer *et al.* [4,5], with extensions and changes to the low-temperature dimethyl ether oxidation mechanism made by us here, was used as input for CHEMKIN [25]. The mechanism developed by Fischer *et al.* contains 82 chemical species and 351 elementary reactions, including H_2/O_2 and CO oxidation, reactions of species containing one to two carbons, and the dimethyl ether submechanism (which is of the most interest here). The changes and extensions to the rate constants of the reactions considered here were calculated (as described above) from steady-state RRKM/master equation calculations with a pressure of 10 atm and fitted with Equation (4) to obtain the temperature dependence of the rate constant over 298–2000 K. Thermodynamic parameters (heat capacity, enthalpy, and entropy)

for species added to this mechanism (nine new species discussed later) were calculated as a function of temperature in the NASA format [34] from our DFT-B3LYP total energies, harmonic vibrational frequencies, and optimised geometries using KHIMERA. Since the heat of formation is calculated as the atomisation energy at 0 K, the heat of formation had to be adjusted to reflect the desired heat of formation at 298 K. Rate expressions for elementary reactions considered here were then added to the mechanism of Fischer *et al*. [4].

The complex kinetics of low-temperature dimethyl ether combustion was modelled with the AURORA package included in the CHEMKIN v3.7.1 kinetics suite [25]. We chose reactor conditions simulating a homogeneous, constant-volume perfectly stirred reactor (PSR) with temperature and pressure conditions held constant, in accord with the modeling work of Curran and coworkers [4,5,9]. A 29.5 cm^3 PSR volume was specified, in accord with the jet-stirred reactor (JSR) experiments of Dagaut *et al*. [35]. Temperature was varied from 550 to 800 K. Pressure was held fixed at 10 atm, and a one-second residence time (τ) was chosen in accord with the experiments of Dagaut *et al*. [35]. For all simulations, dimethyl ether comprised 0.2% of the model mixture in accord with the experiments of Dagaut *et al*. [36]. Two equivalence ratios (again corresponding to experimental conditions of Dagaut *et al*. [35]) were selected for a model reactant mixture comprised of dimethyl ether (fuel), oxygen (oxidiser), and nitrogen (diluent): a stoichiometric ($\phi = 1.0$) composition and a fuel-lean composition ($\phi = 0.2$).

3. Results and discussion

First, we discuss key unimolecular and bimolecular reaction kinetics. We will present earlier estimates made for high-pressure-limit rate constants for each reaction considered, followed by our predicted high-pressure rate constant expressions for these reactions (listed in Tables 1–4). High-pressure rate constants were calculated at specific temperatures for comparison with known literature rates. For the chain-propagation reactions, a temperature of 298 K was chosen because the most prominent experiments on the chain propagation reactions [6,7,37–39] were conducted around room temperature. For chain branching reactions, a temperature of 600 K was chosen because peak amounts of chain branching products were produced around 600 K in the reactor experiments of Dagaut *et al*. [36], Curran *et al*. [5], and Liu *et al*. [8]. Since the comprehensive model of Fischer *et al*. [4,5] includes only high-pressure limit rate constant estimates for the chain propagation and branching reactions considered here, finite pressure rates were calculated for pressures of 1, 10, and 40 atm (covering the range of diesel conditions of compressed gas prior to combustion). Since the experimental conditions we wish to model in the global kinetics are those of Dagaut *et al*. [36], only the 10 atm rate expressions are included in the mechanism. The 1, 10, and 40 atm pressure rate expressions are included as supplemental information.

Reactions of ethylene ozonolysis are included in the comprehensive mechanism of low-temperature DME oxidation by Fischer *et al*. [4,5]. Experimental high-pressure limit rates are unknown for these reactions. Conditions for known experiments are around the standard conditions of 298 K and 1 atm [40–54]. Considerations at higher temperatures and pressures have never been made for these reactions, but will be considered here in the low-temperature combustion of dimethyl ether.

Second, we discuss these reactions in a broader context by including them in a multi-reaction mechanism to look at the global kinetics of dimethyl ether combustion.

3.1. *Unimolecular and recombination reactions in chain propagation*

The first step toward auto-oxidation of dimethyl ether is the removal of a hydrogen by (most likely) molecular oxygen, which begins to occur around 530 K [5,8]. The $CH_3O\dot{C}H_2$ resulting from abstraction then may collide with another O_2 to form a peroxy radical:

$$CH_3O\dot{C}H_2 + O_2 \rightleftharpoons CH_3OCH_2OO\cdot. \qquad (6)$$

The forward reaction of Equation (6) is the first step toward chain propagation, where one highly reactive radical is created, which may create another chain by reacting with another DME molecule. Chain-propagation is depicted (in green) in Figure 1. Sehested *et al*. [6] used smog-chamber techniques to show that the chain-propagation reaction involves a Lindemann-type mechanism. In this mechanism, $CH_3OCH_2OO\cdot$ formed is vibrationally excited (because this is an exothermic radical–radical collision) and can: (1) decompose back into $CH_3O\dot{C}H_2$ and O_2 (indicated by the left arrow in Equation (6)); (2) undergo further reaction; or (3) stabilise via collisions with the bath gas. Previous quantum chemical studies [2,10], have indicated that the addition of O_2 to $CH_3O\dot{C}H_2$ appears to be a 'barrierless' reaction, which will have a loose transition state. Therefore, we have calculated rate expressions for the forward and reverse reactions in Equation (6) using both KHIMERA and VARIFLEX.

Table 1. High-pressure rate expressions in the form of Equation (4) for primary unimolecular and recombination reactions involved in dimethyl ether oxidation chain propagation. Unimolecular reaction rate coefficients are in s^{-1} and recombination (or association) rate coefficients are in $cm^3\,mol^{-1}\,s^{-1}$. '−' in front of an equation number indicates the reverse reaction. Activation energies are in $kcal\,mol^{-1}$.

Reaction (equation #)	$k_\infty(T)$ (this work[a])	k_∞(298 K) (this work)	k_∞ (literature)	k_∞(298 K) (literature)
Primary propagation reactions				
(6)[b]	$2.98 \times 10^{12} T^{0.50}$	5.14×10^{13}	$3.39 \times 10^{11} e^{+1.7/RT}$[c]	5.98×10^{12}
			$6.44 \times 10^{12} e^{+0.1/RT}$[d]	7.62×10^{12}
			$1.87 \times 10^{12} e^{+0.6/RT}$[e]	5.15×10^{12}
			5.82×10^{12}[f]	5.82×10^{12}
			2.00×10^{12}[g]	2.00×10^{12}
−(6)[b]	$1.79 \times 10^{21} T^{-1.26} e^{-30.8/RT}$	3.53×10^{-5}	$1.58 \times 10^{15} e^{-33.4/RT}$[h]	5.06×10^{-10}
			$4.44 \times 10^{19} T^{-1.59} e^{-36.2/RT}$[i]	1.46×10^{-11}
(7)	$9.22 \times 10^{9} T^{0.72} e^{-24.3/RT}$	8.42×10^{-7}	$1.10 \times 10^{7} T^{1.21} e^{-17.1/RT}$[j]	3.12×10^{-3}
			$6.00 \times 10^{10} e^{-21.6/RT}$[g]	8.66×10^{-6}
−(7)	$2.26 \times 10^{11} T^{0.22} e^{-11.8/RT}$	1.76×10^{3}	$1.25 \times 10^{12} e^{-11.2/RT}$[j]	7.64×10^{3}
(8)	$2.08 \times 10^{12} T^{0.51} e^{-11.4/RT}$	1.66×10^{5}	$1.81 \times 10^{12} T^{0.38} e^{-21.0/RT}$[j]	6.27×10^{-3}
			$1.50 \times 10^{13} e^{-20.8/RT}$[g]	8.36×10^{-3}
Competing reaction to $CH_3O\dot{C}H_2 + O_2$ addition				
(9)	$1.70 \times 10^{12} T^{0.71} e^{-22.1/RT}$	6.02×10^{-3}	$1.6 \times 10^{13} e^{-25.4/RT}$[k]	3.77×10^{-6}
Alternative CH_2OCH_2OOH dissociation reactions				
(10)	$3.24 \times 10^{12} T^{0.31} e - 23.7/RT$	7.89×10^{-5}		
(11)	$2.00 \times 10^{12} T^{0.45} e^{-52.8/RT}$	4.93×10^{-26}		

[a]Calculated with KHIMERA [19,20] using DFT-B3LYP//6-311G** results [2].
[b]Loose transition state treated with KHIMERA's Gorin model.
[c]Discharge experiments of Hoyermann and Nacke [37].
[d]Smog-chamber experiments of Sehested *et al.* [7].
[e]Laser photolysis experiments of Maricq *et al.* [39].
[f]Rate constant for $CH_3CH_2CH_2 + O_2$ from Atkinson *et al.* [55] (reference 27 in Yamada *et al.* [10]).
[g]Estimation of Curran and coworkers [4,5].
[h]Microscopic reversibility of Atkinson *et al.* [55] (reference [27]) forward rate constant by Yamada *et al.* [10].
[i]Microscopic reversibility of forward rate expression estimated by Curran and coworkers [4,5].
[j]High-pressure rate expression calculated from CBS-q/MP2//6-31(d,p) results by Yamada *et al.* [10].
[k]Mercury-sensitised photolysis of Loucks and Laidler [65].

Table 2. Varshni parameters (see Equation (5)) for the simple-fission reactions considered in this work.

Equation	Reaction	$D_e(cm^{-1})$	R_e(Å)	$\beta(Å^{-2})$
(6)	$CH_3O\dot{C}H_2 + O_2 \rightleftharpoons CH_3OCH_2OO\cdot$	11,637[a]	1.470	0.642
−(6)	$O_2 + \cdot CH_2OCH_2OOH \rightleftharpoons \cdot OOCH_2OCH_2OOH$	11,875[b]	1.480	0.591
(16)	$HOOCH_2OC(=O)H \rightarrow \cdot OH + \cdot OCH_2OC(=O)H$	16,751	1.452	0.662

[a]$D_e = 13{,}842\,cm^{-1}$, adjusted to the heats of formation (for $CH_3O\dot{C}H_2$ and $CH_3OCH_2OO\cdot$) estimated via group additivity by Curran *et al.* [4,5].
[b]$D_e = 13{,}701\,cm^{-1}$, adjusted to the heats of formation (for $\cdot CH_2OCH_2OOH$ and $\cdot OOCH_2OCH_2OOH$) estimated via group additivity by Curran *et al.* [4,5].

Results calculated with KHIMERA appear in Table 1, while those from VARIFLEX appear in Table 3.

High-pressure rate expressions for the forward reaction of Equation (6) extrapolated from experimental data have been published by Hoyermann and Nacke [37] (3.39×10^{11} exp(+1.7 kcal mol^{-1}/RT) $cm^3\,mol^{-1}\,s^{-1}$, 302–473 K), Sehested *et al.* [7] (6.44×10^{12} exp(+0.1 kcal mol^{-1}/RT) $cm^3\,mol^{-1}\,s^{-1}$, 296–473 K) and Maricq *et al.* [39] (1.87×10^{12} exp ×(+0.6 kcal mol/RT) $cm^3\,mol^{-1}\,s^{-1}$, 220–355 K). The rate coefficient in Equation (6) estimated by Curran *et al.* [4,5] in their modeling of DME combustion products from their variable-pressure flow reactor (VPFR) experiments is

Table 3. High-pressure modified-Arrhenius rate expressions for reactions involving 'loose' (bond-breaking/bond-forming) transition states calculated with the VARIFLEX code [26]. Unimolecular reaction rate coefficients are in s^{-1} and recombination (or association) rate coefficients are in $cm^3\,mol^{-1}\,s^{-1}$. '−' in front of an equation number indicates the reverse reaction. Activation energies are in $kcal\,mol^{-1}$.

Equation	Reaction	k_∞ (expression)	k_∞(298 K)
(6)	$CH_3O\dot{C}H_2 + O_2 \rightarrow CH_3OCH_2OO\cdot$[a]	$6.18 \times 10^{10} T^{0.69} e^{+1.2/RT}$	2.35×10^{13}
−(6)	$CH_3OCH_2OO\cdot \rightarrow CH_3OCH_2 + O_2$[b]	$3.59 \times 10^{19} T^{-1.03} e^{-29.5/RT}$	2.37×10^{-5}
			k_∞(600 K)
(12)	$O_2 + \cdot CH_2OCH_2OOH \rightarrow \cdot OOCH_2OCH_2OOH$[c]	$8.22 \times 10^{9} T^{0.94} e^{1.4/RT}$	1.06×10^{13}
−(12)	$\cdot OOCH_2OCH_2OOH \rightarrow \cdot CH_2OCH_2OOH + O_2$[d]	$1.00 \times 10^{19} T^{-0.71} e^{-30.0/RT}$	1.29×10^{6}
(16)	$HOOCH_2OC(=O)H \rightarrow \cdot OH + \cdot OCH_2OC(=O)H$	$2.29 \times 10^{20} T^{-1.25} e^{-42.7/RT}$	2.14×10^{1}

[a]For the adjusted potential depth (see text), $k_\infty = 2.19 \times 10^{11} T^{0.537} \exp(+1.1/RT)\,cm^3\,mol^{-1}\,s^{-1}$($k_\infty$(298 K) = $2.99 \times 10^{13}\,cm^3\,mol^{-1}\,s^{-1}$).
[b]For the adjusted potential depth (see text), $k_\infty = 1.27 \times 10^{20} T^{-1.178} \exp(-35.9/RT)\,s^{-1}$($k_\infty$(298 K) = $7.2 \times 10^{-10}\,s^{-1}$).
[c]For the adjusted potential depth (see text), $k_\infty = 3.61 \times 10^{10} T^{0.753} \exp(+1.4/RT)\,cm^3\,mol^{-1}\,s^{-1}$($k_\infty$(600 K) = $1.44 \times 10^{13}\,cm^3\,mol^{-1}\,s^{-1}$).
[d]For the adjusted potential depth (see text), $k_\infty = 4.37 \times 10^{19} T^{-0.888} \exp(-35.9/RT)\,s^{-1}$($k_\infty$(600 K) = $1.25 \times 10^{4}\,s^{-1}$).

Table 4. High-pressure rate expressions in the form of Equation (4) for primary unimolecular and recombination reactions involved in chain branching. Unimolecular reaction rate coefficients are in s^{-1} and recombination (or association) rate coefficients are in $cm^3\,mol^{-1}\,s^{-1}$. '−' in front of an equation number indicates the reverse reaction. Activation energies are in $kcal\,mol^{-1}$.

Reaction (equation #)	$k_\infty(T)$ (this work[a])	k_∞(600 K) (this work)	k_∞ (literature[b])	k_∞(600 K) (literature)
Primary branching reactions				
(12)[c]	$2.69 \times 10^{12} T^{0.50}$	6.59×10^{13}	7.00×10^{11}	7.00×10^{11}
−(12)[c]	$3.94 \times 10^{21} T^{-1.19} e^{-31.4/RT}$	7.12×10^{6}	$1.92 \times 10^{19} T^{-1.62} e^{-36.3/RT}$[d]	3.64×10^{1}
(13)	$2.32 \times 10^{11} T^{0.81} e^{-22.9/RT}$	1.88×10^{5}	$4.00 \times 10^{10} e^{-18.6/RT}$	6.72×10^{3}
(15)	$2.99 \times 10^{11} T^{1.01} e^{-43.3/RT}$	3.24×10^{-2}		
(16)	$3.99 \times 10^{20} T^{-0.84} e^{-43.2/RT}$	3.41×10^{2}	$2.00 \times 10^{16} e^{-40.5/RT}$	3.54×10^{1}
Competing HPMF decomposition reactions[e]				
(22)[f]	$2.71 \times 10^{12} T^{0.80} e^{-43.3/RT}$	7.65×10^{-2}		
(23)[f]	$1.58 \times 10^{13} T^{0.37} e^{-28.8/RT}$	5.45×10^{3}		
(25)	$1.38 \times 10^{11} T^{1.02} e^{-51.6/RT}$	1.51×10^{-5}		
(26)	$3.84 \times 10^{10} T^{1.35} e^{-62.3/RT}$	4.39×10^{-9}		
Decomposition reactions of short-lived intermediates				
(24)	$1.18 \times 10^{23} T^{-2.23} e^{-14.9/RT}$	2.81×10^{11}		
(17)	$3.03 \times 10^{11} T^{0.30} e^{-12.0/RT}$	8.79×10^{7}	$1.00 \times 10^{11} e^{-14.0/RT}$	7.95×10^{5}
(21)	$3.56 \times 10^{11} T^{0.34} e^{-3.7/RT}$	1.41×10^{11}		
(27)	$2.80 \times 10^{11} T^{0.55} e^{-26.5/RT}$	2.10×10^{3}		
(28)	$6.13 \times 10^{11} T^{0.48} e^{-32.4/RT}$	2.09×10^{1}		
(29)	$8.11 \times 10^{12} T^{0.10} e^{-21.3/RT}$	2.68×10^{5}		
(30)	$3.22 \times 10^{12} T^{0.42} e^{-18.9/RT}$	6.17×10^{6}		
(31)	$1.42 \times 10^{13} T^{0.11} e^{-2.9/RT}$	2.52×10^{12}		
(32)	$1.68 \times 10^{12} T^{0.33} e^{-1.2/RT}$	5.07×10^{12}		
(33)	$1.27 \times 10^{11} T^{1.02} e^{-66.9/RT}$	3.71×10^{-11}		
(34)	$2.55 \times 10^{10} T^{0.97} e^{-66.5/RT}$	7.57×10^{-12}		

[a]Calculated with KHIMERA [19,20].
[b]Estimated fit to experimental data in comprehensive DME combustion model of Curran and coworkers [4,5].
[c]Loose transition state treated with KHIMERA's Gorin model.
[d]Microscopic reversibility of forward rate expression by Curran and coworkers [4,5].
[e]Reactions not leading to the production of a second ·OH.
[f]Note that $\dot{C}H_2OO$ may decompose to $H\dot{C}O$ and ·OH radicals.

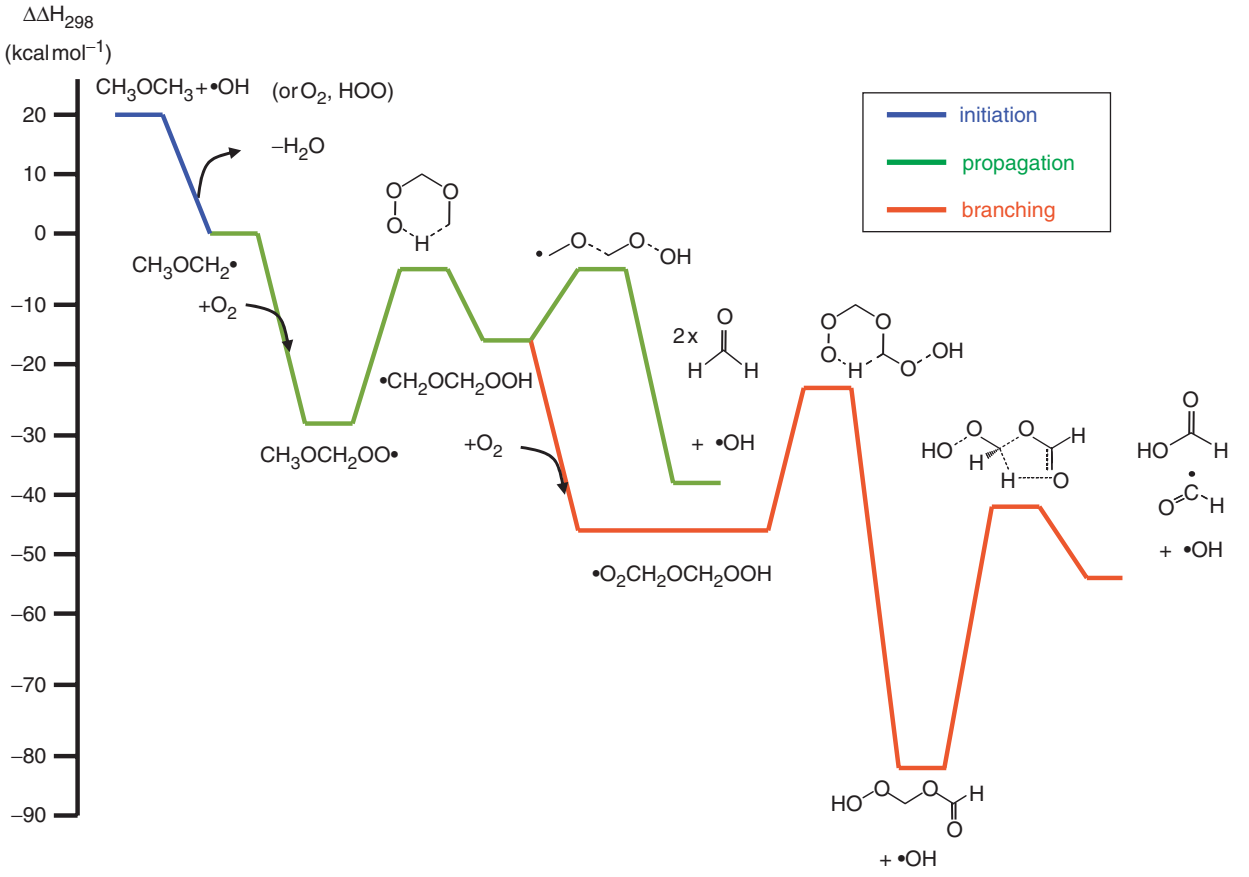

Figure 1. Temperature- and zero-point-corrected enthalpies relative to $CH_3OCH_2 + O_2$ for the initiation (by ·OH), propagation, and branching steps of the chain-branching mechanism involved in DME's low-temperature autoignition.

$2.00 \times 10^{12}\,cm^3\,mol^{-1}\,s^{-1}$, which is about three times lower than the high-pressure rate constant extracted from smog-chamber data at 296 K [6]. Curran *et al.* assume that this is a barrierless reaction. Thus, this rate constant purely reflects the *A*-factor. No temperature dependence (T^n) was specified for this rate constant.

The reverse decomposition reaction was calculated by Curran and coworkers [4,5] from the forward rate using microscopic reversibility (from the thermochemistry of the species involved in Equation (6)). This reverse rate expression is $4.44 \times 10^{19} T^{-1.59}$ $\exp(-36.2\,kcal\,mol^{-1}/RT)\,s^{-1}$. Yamada *et al.* [10] have modeled a subset of low-temperature DME combustion reactions, essentially modeling only the propagation path using (primarily) CBS-q calculated energies and MP2/6-31G(d,p) geometries and frequencies to calculate rate constants. The high-pressure rate constant for the forward reaction that Yamada *et al.* [10] used for the rate constant of Equation (6), $5.82 \times 10^{12}\,cm^3\,mol^{-1}\,s^{-1}$, was taken from reference literature for the analogous $CH_3\dot{C}H_2 + O_2$ reaction [55]. As in the work of Curran *et al.* [4,5], the high-pressure rate expression for the reverse reaction in Equation (6), $1.58 \times 10^{15}\exp(-33.4\,kcal\,mol^{-1}/RT)$, was calculated by Yamada *et al.* from microscopic reversibility. This rate expression does not express any temperature dependence in the *A*-factor, unlike Curran *et al.*'s expression.

The high-pressure rate expression in the forward direction calculated with KHIMERA (Table 1) has an *A*-factor with the same magnitude as those used by Curran *et al.* [4,5] and Yamada *et al.* [10]. However, the result from KHIMERA has a factor of $T^{0.5}$ dependence (which neither Curran *et al.* nor Yamada *et al.* use), which implies an *A*-factor of $5.14 \times 10^{13}\,cm^3\,mol^{-1}\,s^{-1}$ at 298 K. This *A*-factor is an order of magnitude higher than that estimated by Curran *et al.* and Yamada *et al.*

For the reverse reaction of Equation (6), the high-pressure *A*-factor (A_∞) calculated with KHIMERA is almost two orders of magnitude higher than that of Curran *et al.* [4,5] and six orders of magnitude higher than that of Yamada *et al.* [10] (see Table 1). However, if the negative temperature dependence T^n

is included in the A-factor, the A_∞ is predicted to be $1.37 \times 10^{18}\,s^{-1}$ at 298 K, which is roughly three orders of magnitude greater than Yamada *et al.*'s A-factor (which is not temperature dependent) and Curran *et al.*'s temperature-dependent A-factor of $5.17 \times 10^{15}\,s^{-1}$ at 298 K. The activation energy in the high-pressure rate expression calculated with KHIMERA (30.8 kcal mol^{-1}) is about 2.6 kcal mol^{-1} lower than the activation energy calculated by Yamada *et al.* [10] via CBS-q/MP2//6-31G(d,p) isodesmic reactions and microscopic reversibility, and it is 5.2 kcal mol^{-1} lower than calculated by Curran *et al.* [4,5] with group additivity (GA) methods [56–58] and microscopic reversibility. The reason for the discrepancy between our activation energy from KHIMERA using our DFT-B3LYP information and that of Curran *et al.* [4,5] and Yamada *et al.* [10] may be due to the inability of single-reference DFT to sufficiently describe the multi-reference character of diradical oxygen, as mentioned before in the case of the $CH_3CH_2 + O_2$ system [59]. We note also, though, that the CBS-q method is also a single-reference-based technique that, in principle, may also have trouble describing O_2.

For more accurate calculations of the rate constants of Equation (6), we used microcanonical E/J-resolved variational/flexible RRKM theory (VRRKM), as implemented in VARIFLEX [26]. To get better activation energy agreement with the enthalpy of reaction of Equation (6) calculated by Curran *et al.* [4,5] and Yamada *et al.* [10], we also calculated the rate expression with an adjustment of the Varshni potential depth (D_e) to a depth consistent with the heats of formation of the species in Equation (6) published by Curran *et al.* The parameters of this Varshni fit to the C–O scission process appear in Table 2, and the high-pressure rate expression appears in Table 3.

A comparison of high-pressure rate expressions reported by the authors mentioned above with the rate expressions calculated by us appears in Figure 2. As expected, the rate expressions we calculated with VRRKM are closer to the experimental high-pressure rate constants than the rate constants we calculated with the simple Gorin model in KHIMERA, because we employ a better description of the interaction potential and the distance is allowed to vary with temperature in the VRRKM calculations. The calculated VRRKM rate expressions using unadjusted (from the DFT-UB3LYP calculations) D_e were closest to experiment. The unadjusted D_e underestimates the depth of the potential well for $CH_3OCH_2OO\cdot$, according to the heat of reaction implied by the heats of formation for $CH_3O\dot{C}H_2$ and $CH_3OCH_2OO\cdot$ of Curran *et al.* [5]. Thus, this potential well is less

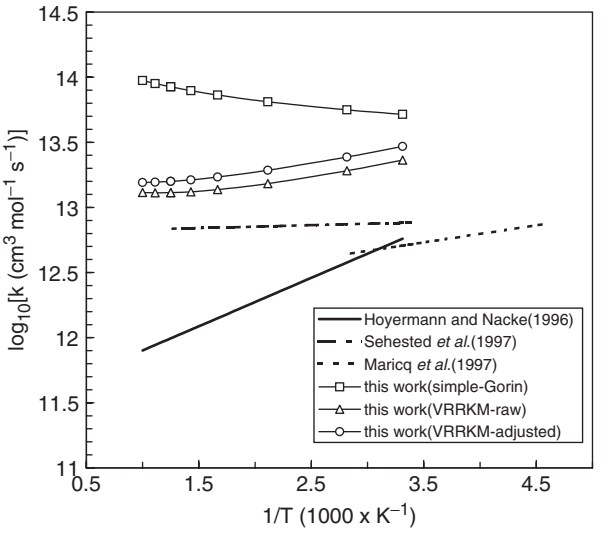

Figure 2. Comparison of rate coefficients for the $CH_3O\dot{C}H_2 + O_2$ reaction (Equation (6)), calculated with KHIMERA (simple Gorin model) and VARIFLEX (VRRKM). VARIFLEX-calculated rate coefficients are reported using the raw DFT-B3LYP D_e results and the D_e adjusted according to the calculated heat of formation of Curran *et al.* [4,5]. The predicted rate coefficients in this work are higher than all measurements, but are closest to those of Sehested *et al.* [7]. Note only the VRRKM predictions get the sign of the slope correct compared to experiment, illustrating the need to variationally optimise loose transition states.

'attractive' compared with the potential well with the adjusted D_e. Therefore, a lower rate would be expected from the unadjusted D_e case, as observed.

High-pressure rate coefficients from VRRKM calculations are still quite a bit higher than the high-pressure rate constants from experiment. This is perhaps due to an incomplete picture of the bond-breaking process. To reduce this rate further, a more complete picture should include an accurate representation of the bending motion orthogonal to the reaction coordinate that changes along the reaction coordinate as the fragments come apart in the bond fission process. Such techniques are being developed by Miller *et al.* [60,61]. In addition to an accurate representation of the bending potential, Wagner *et al.* [62] mentioned, in their variational RRKM analysis of the transition state for an analogous system (addition of O_2 to CH_3CH_2), that the reaction coordinate is likely to be complicated by several curve-crossings involving interactions between O_2 excited states and the neutral $CH_3CH_2 + O_2$ and ionic $CH_3CH_2^+ + O_2^-$ (the latter revelation on ionic states was credited to the work of Ruiz and Bayes [63]). They noted that their final fitted Morse parameters for this reaction were more consistent with a relatively

shallow and broad potential, consistent with a potential surface containing a mixture of ground, excited, and ionic states rather than a relatively deep and narrow well expected for a simple bond-breaking process.

Rather than decomposing back into $CH_3O\dot{C}H_2$ and O_2, the $CH_3OCH_2OO\cdot$ radical can undergo a unimolecular isomerisation:

$$CH_3OCH_2OO\cdot \rightleftharpoons \cdot CH_2OCH_2OOH. \qquad (7)$$

This is an endothermic process, and it is possible that if $\cdot CH_2OCH_2OOH$ stabilises, the reverse isomerisation reaction could also occur. This reaction has a well-defined transition state that is much tighter than that found for addition of O_2 to $CH_3O\dot{C}H_2$. Our high-pressure rate constant for reaction (7) appears in Table 1. Yamada's high-P rate constant for this reaction is $1.10 \times 10^7\ T^{1.21}\ \exp(-17.1\,\text{kcal mol}^{-1}/RT)$. Their A_∞-factor ($1.08 \times 10^{10}\,s^{-1}$) suggests a 'tighter' transition state than does our A_∞ ($5.57 \times 10^{11}\,s^{-1}$) at 298 K. This may be due to a lack of hindered rotor treatment for CH_3–O–CH_2–$OO\cdot$ by us or a difference between our DFT-B3LYP//6-311G** structures and frequencies and the MP2/6-31G** structures and frequencies of Yamada *et al.* (or a combination of both) [10]. However, their activation energy is 7.2 kcal mol^{-1} lower than our activation energy (interesting, since DFT-B3LYP has the reputation of underestimating transition state barriers; not so for CBS-q and MP2). They also have a more pronounced positive temperature dependence in the pre-exponential, which may be due to our lack of hindered rotor treatment in the partition functions (especially when we are dealing with a somewhat floppy molecule undergoing a cyclic transition where the hindered rotations of $CH_3OCH_2OO\cdot$ should not be neglected). Hindered rotor treatment would be difficult to perform with the systems considered here. An analysis of the normal mode displacements reveals low frequency normal modes that cannot be easily assigned to specific rotations about the bonds considered to have free rotation (because of mode mixing). Moreover, the large molecules studied here have many conformations. However, Ayala and Schlegel [64] are developing promising methods for accurate hindered rotor treatment using information from redundant internal coordinates available from a standard *ab initio* optimisation calculation, which may be of use in future work.

The activation energy definitely has the greatest effect on the rate of reaction (7). The rate constant is about $3.12 \times 10^{-3}\,s^{-1}$ at 298 K according to Yamada *et al.* and $8.42 \times 10^{-7}\,s^{-1}$ at 298 K from our calculations with KHIMERA. Curran *et al.* [5] seemed to have used a high-pressure rate expression and activation energy in between our rate expression and activation energy and those of Yamada *et al.* [10] Curran *et al.* [5] estimated the bond energy through an empirical expression involving ring-strain, hydrogen abstraction, and the enthalpy of reaction [5]. Their *A*-factor was chosen from an analogous ring-shaped isomerisation transition state in their model of *n*-heptane oxidation. According to Gilbert and Smith [22], our A_∞-factor at 298 K is closer to the appropriate range of $10^{11.5-15}\,s^{-1}$ for five- and six-membered cyclic transition states. The rate constant at 298 K using Curran *et al.*'s expression is $8.66 \times 10^{-6}\,s^{-1}$. A comparison of our calculated rate expression over a temperature range of 300–1000 K for reaction (7) with those of Yamada *et al.* [10] and Curran *et al.* [4,5] appears in Figure 3, which clearly shows that our rate expression agrees better with Curran *et al.*'s rate expression than with that of Yamada *et al.* Also, we see that our rate coefficients are lower than Curran *et al.*'s rate constants at the low-end of the temperature scale and higher at higher temperatures.

After CH_2OCH_2OOH is formed through Equation (7), CH_2OCH_2OOH can decompose to form one $\cdot OH$ and two formaldehyde molecules to complete the propagation chain

$$\cdot CH_2OCH_2OOH \rightarrow 2H_2C{=}O + \cdot OH. \qquad (8)$$

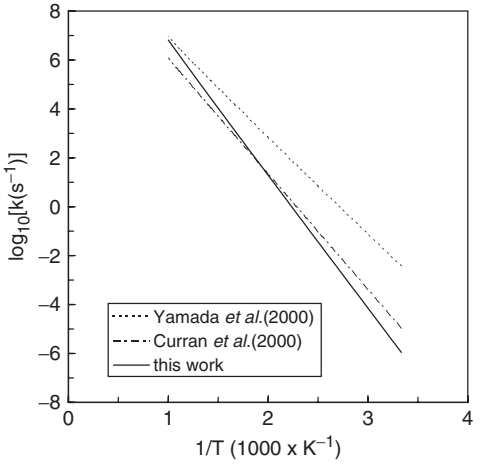

Figure 3. Comparison for the rate coefficients for the isomerisation of $CH_3OCH_2OO\cdot$ (Equation (7)) with literature estimates of the rate coefficients. Our predicted values are closest to that of Curran *et al.* [4,5]. However, our rate coefficients are lower than Curran *et al.*'s at temperatures below about 500 K, and higher above about 500 K (approaching those of Yamada *et al.* [10]).

We predict a high-pressure rate expression of $2.08 \times 10^{12} T^{0.51} \exp(-11.4\ \text{kcal mol}^{-1}/RT)$, whereas Yamada *et al.* [10] calculated a high-pressure rate expression of $1.81 \times 10^{12}\ T^{0.38} \exp(-21.0\ \text{kcal mol}^{-1}/RT)\ \text{s}^{-1}$. There is a positive temperature dependence in the pre-exponential in both cases, with our result being a bit more pronounced. As mentioned in our previous work [2], we found a transition state that differs from that of Yamada *et al.* They found a transition state where CH_2O–CH_2OOH is the breaking bond (CH_2OOH readily decomposes to $H_2C{=}O$ and ·OH). The transition state we found has the CH_2OCH_2O–OH bond breaking. The CH_2OCH_2O readily breaks apart into two formaldehyde molecules. In the work of Yamada *et al.*, they had to decrease their activation energy about $3\ \text{kcal mol}^{-1}$ to get good agreement with experiment in their QRRK calculations. Curran *et al.* [4,5] suggested a 1.50×10^{13} $\exp(-20.8\ \text{kcal mol}/RT)$ high-pressure rate constant for this reaction. They calculated this rate constant via microscopic reversibility of the known rate constant for a methyl radical added across the double bond of ethylene to yield *n*-propyl. They reasoned that methyl radical addition to ethylene was similar to the bond-formation behaviour of the reverse reaction of Equation (8). They also noted that they reduced their activation barrier by about $3.0\ \text{kcal mol}^{-1}$ to get their model to agree with experiment.

The rate expression of reaction (8) determined by Yamada *et al.* [10] and Curran *et al.* [4,5] imply that the decomposition reaction (Equation (8)) is the bottleneck to formaldehyde production in chain-propagation. Based on our calculations, instead the isomerisation reaction (7) appears to be the bottleneck along the propagation path. At 298 K, the high-pressure rate constant of the decomposition reaction is $1.66 \times 10^5\ \text{s}^{-1}$. We find that the transition state of reaction (8) has a larger A_∞ factor ($3.80 \times 10^{13}\ \text{s}^{-1}$ at 298 K) than that of reaction (7) ($5.57 \times 10^{11}\ \text{s}^{-1}$ at 298 K), because the former is a disproportionation reaction (decomposition to radical and non-radical species), which typically has a 10^{14}–$10^{15}\ \text{s}^{-1}$ A_∞ factor [22], whereas the latter is an isomerisation reaction involving a six-centered transition state with a much tighter A_∞ factor (typically $10^{11.5}$–$10^{14}\ \text{s}^{-1}$). From previous work [2], we know that the barrier heights of isomerisation reaction (7) and decomposition reaction (8) with respect to $CH_3O\dot{C}H_2 + O_2$ are almost the same. Thus, from the A_∞ alone, we know that reaction (8) is more favourable than reaction (7).

We find that the rate expression for decomposition (Equation (8)), using the transition state found in our previous work, is very sensitive to pressure in the RRKM/master equation calculations. Figure 4 shows the deviation from the high-pressure limit rate constant for three pressures (1, 10, and 40 atm) pertinent to diesel combustion over a temperature range 300–1000 K. Little deviation from the high-pressure limit rate coefficient is seen for the 1, 10, and 40 atm pressure rate coefficients at 300 K. As temperature is increased, the deviation of the 1, 10, and 40 atm rate constants from the high-pressure limit rate constant increases nonlinearly. As expected, the 1 atm rate constant shows the greatest deviation from the high-pressure limit rate constant, with the 40 atm rate constant showing the least deviation. For the pressure-dependent rate constants of reaction (8), deviation from the high-pressure rate constant is obvious at temperatures as low as 400 K. Typically, at fairly low temperatures, we should see a rise to the high-pressure limit by about 1 atm [22]. Thus, the rate constant of decomposition reaction (8) as a function of pressure is atypical. For the rate expression through a 'tighter' transition state such as that of reaction (7), the deviation of the 1, 10, and 40 atm pressure rate constants from the high-pressure limit rate constant is virtually zero over the 300–1000 K temperature range. For the most part, high-pressure rate constants can be assumed for the reactions involved in DME

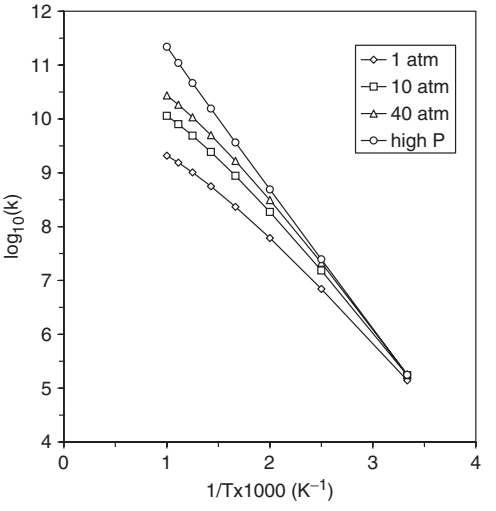

Figure 4. Pressure dependence of the rate coefficients for reaction (8). As the pressure increases, the rate coefficient is expected to approach the high-pressure limit (open circles). 1, 10, and 40 atm rate coefficients increasingly deviate from the high-pressure limit going from 300 to 1000 K (a range pertinent to low-temperature DME combustion), with the 1 atm rate coefficient having the greatest deviation from the high-pressure limit and the 40 atm rate coefficient having the least deviation. Note that deviation from the high-pressure limit is noticeable for all pressures at temperatures 400 K and higher. Thus, pressure dependence is an important consideration in large-scale kinetics modeling.

combustion because of the rather high pressures of diesel combustion, but the pressure sensitivity of the rate of reaction (8) should be accounted for. The pressure dependence of the rate through reaction (8) is an important observation, since the addition of O_2 to $\cdot CH_2OCH_2OOH$ to begin chain branching must compete with the dissociation of $\cdot CH_2OCH_2OOH$ to $2H_2C{=}O + \cdot OH$. The dissociation of $\cdot CH_2OCH_2OOH$ (reaction (8)) demonstrates the need to include pressure-dependent elementary reaction rate expressions in the global mechanism for dimethyl ether combustion.

One final comment concerning reaction (8): Sehested *et al.* [6] concluded that a Lindemann-type mechanism including reactions (6), (7), and (8) explained their observed product yields. Their mechanism seems to assume that $\cdot CH_2OCH_2OOH$ completely dissociates to $2H_2C{=}O$ and $\cdot OH$, implying that the rate of reaction (8) was fast enough at the conditions of their experiment to be neglected. With our unimolecular results alone, the neglect of reaction (8) seems warranted. However, in Section 3.4, we will see that neglect of reaction (8) may not be reasonable.

Earlier, we mentioned that the isomerisation reaction (Equation (7)) may be reversible. The rate constant of the reverse of reaction (7) is $1.76 \times 10^3\,s^{-1}$ at 298 K. But, the competing reaction at 298 K, the decomposition reaction (8), has a rate constant of $1.66 \times 10^5\,s^{-1}$, a couple of orders of magnitude higher than the reverse rate constant of reaction (7). Thus, according to our calculations, reaction (8) is expected to be more prevalent at room temperature than the reverse reaction of Equation (7). This disagrees with the rate coefficients calculated by Yamada *et al.* [10] for the reverse reaction of Equation (7) and reaction (8), which indicate that the reverse of Equation (7) is more prevalent (see Table 1).

We also include some reactions that we explored previously [2] with DFT-B3LYP energetics calculations. The first of these is the unimolecular decomposition of $CH_3O\dot{C}H_2$:

$$CH_3O\dot{C}H_2 \rightarrow \cdot CH_3 + H_2C{=}O. \qquad (9)$$

The barrier to reaction (9) is about $E_a = 22.1\,kcal\,mol^{-1}$ according to our DFT-B3LYP calculations. Reaction (6) will be more favourable at relatively low temperatures (below 1000 K), but the pyrolysis reaction of Equation (9) may compete in the high-temperature combustion of dimethyl ether. Loucks and Laidler [65] derived an activation energy of $E_a = 25.4\,kcal\,mol^{-1}$ from an Arrhenius fit to their photolysis/GC data over a temperature range 373–473 K ($k_\infty = 1.6 \times 10^{13}\exp(-25.4\,kcal\,mol^{-1}/RT)\,s^{-1}$). Our rate expression listed in Table 1 gives a rate constant at 373 K of $k_\infty = 1.31 \times 10^1\,s^{-1}$, which is off from the experimental result at 373 K ($2.0 \times 10^{-2}\,s^{-1}$) by about three orders of magnitude. Sehested [7] used Loucks and Laidler's expression for reaction (9) in their complex mechanism used in modeling their photolysis study from 573 to 666 K. At 573 K, we calculate $k_\infty = 5.90 \times 10^5\,s^{-1}$, much closer to Louck and Laidler's $k_\infty = 3.1 \times 10^5\,s^{-1}$. Our rate constant is only a factor of 2 higher at 573 K, suggesting perhaps that in the regime where this process may be important, namely high temperatures, our rate expression may be fairly reliable.

The final two reactions we consider in this section are the following:

$$\cdot CH_2OCH_2OOH \rightarrow 1,3\text{-dioxetane} + \cdot OH, \qquad (10)$$

$$\cdot CH_2OCH_2OOH \rightarrow \text{ethylene oxide} + HOO\cdot. \qquad (11)$$

Both reactions involve the decomposition of $\cdot CH_2OCH_2OOH$, and both reactions produce a highly reactive radical ($\cdot OH$ in the case of reaction (10) and $HOO\cdot$ in the case of reaction (11)). However, neither reaction is likely to occur because of their high barriers, which are above the relative energies of the $CH_3O\dot{C}H_2 + O_2$ precursors. The high-pressure rate expressions predicted for reactions (10) and (11) appear in Table 1.

3.2. *Unimolecular and recombination reactions in chain branching*

The chain-branching path, which begins with the addition of O_2 to $\cdot CH_2OCH_2OOH$, has not been studied as extensively as the chain propagation path. Group-additivity estimates and transition state rules of thumb for the reactions involved in chain branching have been published by Curran *et al.* [5,9], but no quantum chemistry-derived rate expressions have been calculated. Here we present the unimolecular/recombination rate expressions for the chain-branching path calculated from our DFT-B3LYP results.

3.2.1. *Formation of the first $\cdot OH$*

The chain-branching path starts in an analogous way to the production of the $CH_3OCH_2OO\cdot$ complex in chain-propagation, with an O_2 adding to $\cdot CH_2OCH_2OOH$

$$\cdot CH_2OCH_2OOH + O_2 \rightleftharpoons \cdot OOCH_2OCH_2OOH. \qquad (12)$$

Like Equation (6), Equation (12) is also reversible, has Lindemann-type qualities, and has no well-defined barrier to association (dissociation). The estimated high-pressure rate expression (forward and reverse of reaction (12)) calculated with the simple Gorin model of KHIMERA, with input from DFT-B3LYP calculations, is listed in Table 4. Curran *et al.* [4,5] used $7.0 \times 10^{11}\,cm^3\,mol^{-1}\,s^{-1}$ for the forward rate constant to get favourable agreement with their experimental product yields. Since peak yields of formic acid from chain branching occur around 600 K in the experiments of Curran *et al.* [5] and Liu *et al.* [8], we will compare rate constants at 600 K. Similar to KHIMERA's predictions for Equation (6), KHIMERA's Equation (12) rate constant at 600 K ($6.59 \times 10^{13}\,cm^3\,mol^{-1}\,s^{-1}$) is about two orders of magnitude higher than that used by Curran *et al.* [4,5] ($7.00 \times 10^{11}\,cm^3\,mol^{-1}\,s^{-1}$).

For the reverse of Equation (12), Curran *et al.* calculated via microscopic reversibility the rate expression $1.92 \times 10^{19} T^{-1.62}\ \exp(-36.3\,kcal\,mol^{-1}/RT)\,s^{-1}$. At 600 K, KHIMERA's A_∞ is again (like with Equation (6)) about three orders of magnitude higher than that used by Curran *et al.* As with the activation energies of the calculated rate expression for Equation (6), the activation energy for the reverse of reaction (12) calculated by Curran *et al.* is about $5\,kcal\,mol^{-1}$ higher than our prediction. The reason is the same as for the analogous reaction in Equation (6): the single-reference UDFT-B3LYP does an inadequate job of describing the multi-reference character of O_2, leading to too low a barrier to the reverse of reaction (12).

As with reaction (6), we have done VRRKM calculations with VARIFLEX [26]. These results appear in Table 3 (with the appropriate Varshni parameters in Table 2). We have calculated VRRKM rate expressions with the raw DFT-B3LYP results and with the $\cdot OOCH_2OCH_2OOH$ well depth adjusted to the depth implied by Curran *et al.*'s [4,5] estimated thermochemistry. At 600 K, our rate constant for the forward reaction of Equation (12) of $1.06 \times 10^{13}\,cm^3\,mol^{-1}\,s^{-1}$ is about an order of magnitude higher than Curran *et al.*'s temperature-independent rate constant of $7.00 \times 10^{11}\,cm^3\,mol^{-1}\,s^{-1}$. With the adjustment to the well depth, the rate constant at 600 K from our calculations is $1.44 \times 10^{13}\,cm^3\,mol^{-1}\,s^{-1}$, which is a bit higher than the previous rate constant (unadjusted). This is still too high compared to Curran *et al.* [4,5]. Again, as in the case of reaction (6), more work needs to be done to accurately portray the potential energy surface of reaction (12), including an accurate representation of the bending potential.

The chain-branching path continues with a hydrogen-transfer isomerisation, similar to the isomerisation reaction along the chain-propagation pathway (Equation (7))

$$\cdot OOCH_2OCH_2OOH \rightarrow HOOCH_2O\dot{C}HOOH. \quad (13)$$

Unlike Equation (7), this reaction has only a very slight chance of reversibility in the temperature range in which first-stage chain-branching occurs (550–700 K). It is more likely that the unstable intermediate, $HOOCH_2O\dot{C}HOOH$, dissociates into $HOOCH_2OC(=O)H$ (hydroperoxymethyl formate, HPMF) and $\cdot OH$,

$$HOOCH_2O\dot{C}HOOH \rightarrow HOOCH_2OC(=O)H + \cdot OH, \quad (14)$$

within the first 500 fs of its formation, based on DFT-B3LYP molecular dynamics simulations that are discussed elsewhere [66]. A rough estimate rate constant for reaction (14) using the simple Gorin model as implemented in KHIMERA is $4.64 \times 10^{16}\,s^{-1}$ at 600 K (i.e. a $HOOCH_2O\dot{C}HO$–OH lifetime of 216 fs).

The high-pressure rate constant for reaction (13) appears in Table 4. Curran *et al.* [4,5] estimated this cyclic isomerisation to have a rate expression of $4.00 \times 10^{10}\ \exp(-18.6\,kcal\,mol^{-1}/RT)\,s^{-1}$, based on the best agreement to their experimental data. Our A_∞ at 600 K, $4.05 \times 10^{13}\,s^{-1}$, is about three orders of magnitude larger than that of Curran *et al.*, but our activation energy is a few $kcal\,mol^{-1}$ larger than that of Curran *et al.* Thus, our high-pressure rate constant at 600 K is $1.88 \times 10^5\,s^{-1}$, more than an of order of magnitude higher than Curran *et al.*'s 600 K rate constant of $6.72 \times 10^3\,s^{-1}$. Their rate expression from their previous study [9] has an activation energy of about $7\,kcal\,mol^{-1}$ lower than ours, and an A-factor about two orders of magnitude lower than ours at 600 K. This rate expression from their previous study is $4.29 \times 10^5\,s^{-1}$, which is about twice our rate constant for reaction (13) at 600 K, but, nevertheless, closer to our rate constant than their latest rate constant. This suggests further experimental work is warranted.

3.2.2. *HPMF's multiple decomposition channels and formation of the second ·OH*

In previous work [3], we demonstrated that hydroperoxymethyl formate (HPMF) can have many viable dissociation pathways, which have barriers that vary between 40 and $66\,kcal\,mol^{-1}$. Of course, pathways with barriers around $40\,kcal\,mol^{-1}$ will be the most

likely from an energetics standpoint. However, the A-factor, a measure of transition state 'looseness', can be used to determine which transition state is more kinetically favourable when activation energies are almost equal. Thus we will start by considering, in detail, the transition states that are $\sim$40 kcal mol^{-1} above HPMF.

First, we consider the unimolecular decomposition of HPMF directly into formic acid (HC(=O)OH), $H\dot{C}O$, and ·OH:

$$HOOCH_2OC(=O)H \rightarrow HC(=O)OH + H\dot{C}O + \cdot OH. \quad (15)$$

The above reaction has an activation barrier $E_a = 43.3$ kcal mol^{-1}, according to our calculations. The reaction of Equation (15) was mentioned and discussed recently in our work [3] and by Curran *et al.* [5]. They estimated that this reaction has a 40–45 kcal mol^{-1} barrier with an A-factor on the order of 10 [14] s^{-1}. The high-pressure rate expression for reaction (15) that we find with KHIMERA appears in Table 4. Our pre-exponential shows quite a bit of positive temperature dependence. The A_∞-factor is 1.96×10^{14} s^{-1} at 600 K. The reaction of Equation (15) falls into two reaction-type categories, disproportionation (one closed-shell species and two radical species) and one with a five-centered cyclic transition state. This A_∞-factor falls into the range appropriate for a typical unimolecular disproportionation reaction (10^{14}–10^{15} s^{-1}) and a five-membered cyclic transition state ($10^{11.5}$–10^{15} s^{-1}) [22].

The A_∞-factor of reaction (15) is small compared to a typical A_∞-factor for a simple-scission reaction where one bond breaks. A typical simple-scission process has an A_∞-factor in the range 10^{16}–$10^{17.5}$ s^{-1} [22]. Curran *et al.* [5] are in favour of simple scission of the O–O peroxide bond in HPMF to form $\cdot OCH_2OCHO$ and ·OH, and have used this in their modeling of low-temperature DME oxidation:

$$HOOCH_2OC(=O)H \rightarrow \cdot OCH_2OC(=O)H + \cdot OH. \quad (16)$$

They argued that reaction (15) would not be as competitive with O–O scission because a loose scission reaction will have a higher A_∞-factor than the tighter transition state of reaction (15). They estimated their rate expression from the work of Sahetchian *et al.* [67], where a typical RO–OH homolysis reaction is 1.0×10^{16} exp(−43.0 kcal mol^{-1}/RT) s^{-1}. Curran *et al.* adjusted this to 2.0×10^{16} exp(−40.5 kcal mol^{-1}/RT) to obtain good agreement with their experiments. In our recent work [3], we calculated this endothermic reaction to have $\Delta H_{rxn}(298\,K) = 41.9$ kcal mol^{-1}. Since simple-scission reactions such as reaction (16) are usually considered 'barrierless' (i.e. lack a true saddle-point structure) and thus have a 'loose' transition state, we again used the VARIFLEX code [26] to calculate this rate variationally. Parameters appear in Table 2 for the Varshni potential used, and the resultant rate expression appears in Table 3. At 600 K, our rate constant of 2.14×10^1 s^{-1} is only slightly smaller than the 3.54×10^1 s^{-1} rate constant derived by Curran *et al.* [5]. The rate constant at 600 K (3.41×10^2 s^{-1}) calculated with KHIMERA is an order of magnitude higher than either k_∞(600 K) calculated with VARIFLEX or the rate constant used in Curran *et al.*'s modeling, which shows that a variational scheme is important for these cases with no energy barrier. If we fit the calculated rate constants of VARIFLEX only over the 500–700 K considered by Sahetchian *et al.* [67], the resulting Arrhenius expression is $k_\infty = 2.44 \times 10^{16}$exp(−41.4 kcal mol^{-1}/$RT$) s^{-1}, which has an A-factor and activation energy only slightly higher than those used by Curran *et al.* in their modeling.

Comparing the calculated VRRKM rate constant at 600 K for Equation (16) (2.14×10^1 s^{-1}) with that of Equation (15) (3.24×10^{-2} s^{-1}), we see that Equation (15)'s rate constant is three orders of magnitude lower than that of Equation (16). Thus it seems that the O–O cleavage reaction of Equation (16) is more favourable than the disproportionation reaction of Equation (15), although reaction (15) leads to products that are more thermodynamically stable (net) than the sum of the products produced by reaction (16).

Even if O–O scission is the most likely way that HPMF dissociates, we disagree with the mechanism proposed by Curran *et al.* [5] on how the $\cdot OCH_2OCHO$ radical dissociates. In their mechanism, the $\cdot OCH_2OCHO$ radical undergoes a rather circuitous path beginning with the transfer of the aldehyde hydrogen to the terminal radical oxygen

$$\cdot OCH_2OC(=O)H \rightarrow HOCH_2O\dot{C}O. \quad (17)$$

This step is followed by a dissociation of the $HOCH_2O\dot{C}O$ radical:

$$HOCH_2O\dot{C}O \rightarrow HOCH_2O\cdot + CO, \quad (18)$$

or

$$HOCH_2O\dot{C}O \rightarrow HO\dot{C}H_2 + CO_2. \quad (19)$$

$HOCH_2O\cdot$ will be the most likely source of formic acid:

$$HOCH_2O\cdot \rightarrow H + HC(=O)OH. \quad (20)$$

However, we believe that the direct path proposed by Liu *et al.* [8] where $\cdot OCH_2OC(=O)H$ decomposes in one step forming $H\dot{C}O$ and HC(O)OH is the most plausible route to formic acid formation:

$$\cdot OCH_2OC(=O)H \rightarrow H\dot{C}O + HC(=O)OH. \quad (21)$$

This route accomplishes the same effect as the direct decomposition reaction (15), producing ·OH, $H\dot{C}O$, and HC(=O)OH. However, this route beginning with reaction (16) takes two steps, whereas the route through reaction (15) takes only one step. Our DFT-B3LYP//6-311G** calculations show that the transition state for Equation (21) has an activation barrier $E_a = 3.7\,\text{kcal mol}^{-1}$. With an activation barrier of $E_a = 12.0\,\text{kcal mol}^{-1}$, reaction (17) has a barrier about $8\,\text{kcal mol}^{-1}$ higher (geometry shown in Figure 5(b)). Moreover, Equation (21)'s A_∞ is slightly larger than that of Equation (17) (see Table 4), which further indicates that the rate of Equation (21) will be higher than Equation (17).

In our previous work [3], we found that the Criegee intermediate of ethylene ozonolysis (i.e. carbonyl oxide, CH_2OO) may be one of the dissociation products of HPMF in addition to formic acid. We found two HPMF dissociation channels leading to one formic acid molecule and one carbonyl oxide diradical (or zwitterion):

$$HOOCH_2OC(=O)H \rightarrow HC(=O)OH + \cdot CH_2OO\cdot. \quad (22)$$

The first of these two transition states is a 'tight' five-membered cyclic transition state involving hydrogen transfer and C–O bond scission. The transferring hydrogen is the peroxide hydrogen. The products of reaction (22) also indicate this reaction is a disproportionation reaction. Thus, the rate constant should have an A_∞ factor in the 10^{14}–$10^{15}\,\text{s}^{-1}$ range. The rate expression for this pathway calculated with KHIMERA appears in Table 4.

The second HPMF dissociation path to formic acid and carbonyl oxide formation also involves a hydrogen transfer, but this involves a seven-centered cyclic transition state. However, in our previous work [3], we showed that the H-transfer and subsequent C–O scission is virtually barrierless, and the only detectible saddle point along the reaction path is a rotation of the CH_2OO fragment in a H-bonded $HC(=O)OH\cdots CH_2OO$ complex with C_s symmetry

$$HOOCH_2OC(=O)H \rightarrow HC(=O)OH\cdots CH_2OO. \quad (23)$$

An additional $\sim 14\,\text{kcal mol}^{-1}$ is needed to separate these fragments

$$HC(=O)OH\cdots CH_2OO \rightarrow HC(=O)OH + CH_2OO. \quad (24)$$

The total endothermicity of reactions (23) and (24) (at 298 K) is $42.0\,\text{kcal mol}^{-1}$. The enthalpic barrier for the five-membered cyclic transition state of the Equation (22) reaction is $\Delta H^{\ddagger}_{298} = 43.5$ ($1.5\,\text{kcal mol}^{-1}$ above the endothermicity). However, the seven-membered ring is virtually barrierless, and it is questionable how this reaction should be treated with transition state theories. This transition state can almost be treated with variational transition state theory because of its looseness. But, the hydrogen transfer rearrangement requires the reaction to be somewhat 'tight'

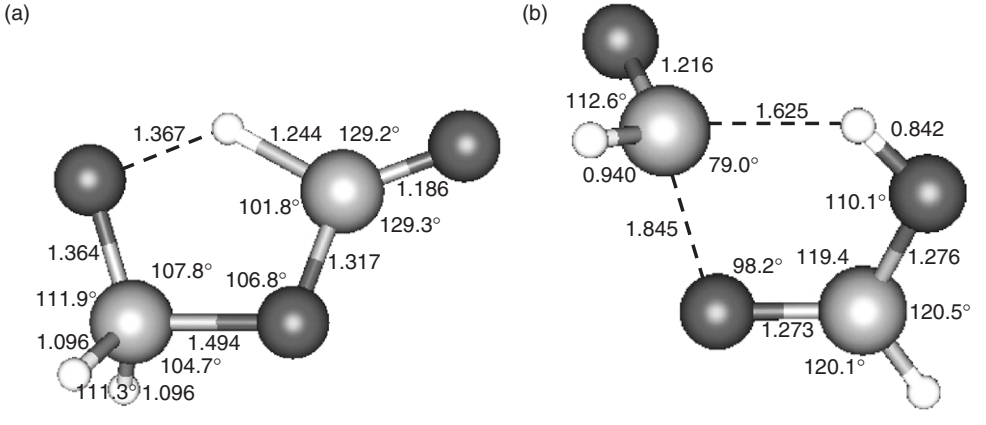

Figure 5. Geometries for the transition states leading to $\cdot OCH_2OC(=O)H$ decomposition: (a) transition state for reaction (17) and (b) transition state for reaction (21). Angle values are indicated with the degree symbol '°' and the values without a degree symbol are bond lengths (in Å). The white balls are hydrogens, the light gray balls are carbons, and the dark gray balls are oxygens.

(i.e. fragments in close proximity). The formic acid and carbonyl oxide also need to be in a specific orientation to recombine. Variational transition state theory also requires that one pivot atom be specified in each fragment species, but the fragments of the formic acid–carbonyl oxide complex are joined at two points and thus require a multi-pivot point treatment. However, the present version of VARIFLEX allows only a single pivot atom treatment. 'Multi-faceted' loose transition states (i.e. 'dividing surfaces') have been treated recently by Georgievskii and Klippenstein [68]. We will treat this as a two-step reaction where (1) the H-transfer with C–O scission forms the H-bonded $HC(=O)OH\cdots CH_2OO$ complex with the saddle-point structure found previously [3] and (2) the $HC(=O)OH\cdots CH_2OO$ separate (barrierlessly) to form individual HC(=O)OH and CH_2OO fragments. At 600 K, the former reaction has a k_∞ of $5.45\times10^3\,s^{-1}$, and the latter reaction has a k_∞ of $2.81\times10^{11}\,s^{-1}$ according to our calculations with KHIMERA. If we treat reaction (22) as just an effective one-step process with no barrier, we obtain $k_\infty(600\,K)=1.63\times10^3\,s^{-1}$. Either way, reaction (22) via the virtually barrierless path may be more favourable than that of O–O scission via Equation (16). A comparison of these HPMF unimolecular reaction rate coefficients is displayed in Figure 6.

The above HPMF decomposition reactions have the lowest barriers to reaction (41–43 kcal mol^{-1}), but there are other possible reactions we mention in passing. These are

$$HOOCH_2OC(=O)H \rightarrow HC(=O)OC(=O)H + H_2O \quad (25)$$

and

$$HOOCH_2OC(=O)H \rightarrow HC(=O)OOH + H_2 + CO. \quad (26)$$

The reaction of Equation (25) is not a favourable decomposition path for HPMF for two reasons: (1) the barrier to reaction is a little greater than 50 kcal mol^{-1}, and (2) the transition state is a very tight four-centered cyclic transition state, which typically has an A_∞ in the range 10^{13}–$10^{14}\,s^{-1}$ [22]. Indeed, reaction (25) has an A_∞ of $8.26\times10^{13}\,s^{-1}$ at 600 K. If HPMF manages to dissociate to H_2O and formic acid anhydride, which are very thermodynamically favourable products ($\Delta H_{rxn}(298\,K)=-58.4$ kcal mol^{-1}), the formic acid anhydride will likely dissociate into formic acid and carbon monoxide:

$$HC(=O)OC(=O)H \rightarrow HC(=O)OH + CO, \quad (27)$$

which has a DFT-B3LYP activation energy of $E_a=26.5$ kcal mol^{-1}.

The reaction of Equation (26) is even less favourable than that of Equation (25) because it requires a little more than 60 kcal mol^{-1} to surmount the barrier to reaction. However, it has a slightly looser transition state structure than that of Equation (25), with an $A_\infty=2.16\times10^{14}\,s^{-1}$ at 600 K, which is typical for a five-centered cyclic transition state ($10^{11.5}$–$10^{15}\,s^{-1}$) [22].

3.2.3. *Bimolecular 'catalysed' decomposition of HPMF*

Aplincourt and Ruiz-López [69] have proposed that HPMF can undergo decomposition into H_2O and formic acid anhydride with the help of 'ancillary' species such as formic acid and H_2O. Aplincourt and Ruiz-López located one transition state structure with DFT-B3LYP in which a formic acid molecule catalyses the decomposition of HPMF into formic acid

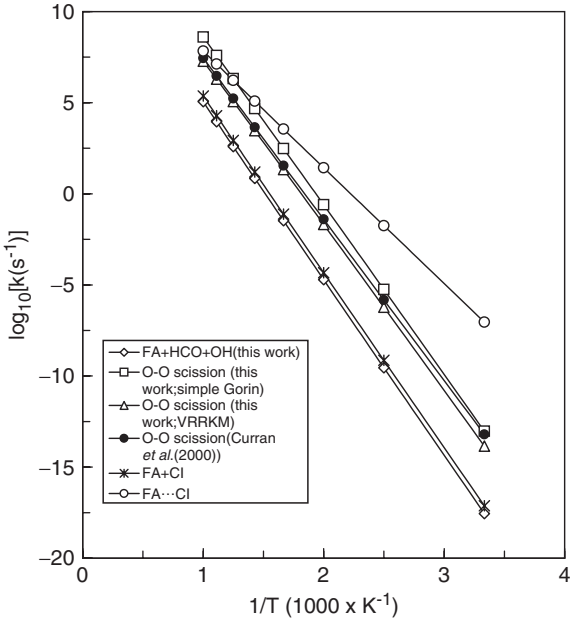

Figure 6. Comparison of the most likely unimolecular decomposition pathways. Note that we show three rate coefficients for decomposition of HPMF via O–O scission (Equation (16)): (1) the rate coefficient calculated with the simple Gorin model, as implemented in KHIMERA [19], (2) the rate coefficient calculated with VRRKM, as implemented in VARIFLEX [26], and (3) the rate coefficient used in Curran *et al.*'s [4,5] complex kinetics model. 'FA' stands for formic acid (HC(=O)OH) and 'CI' stands for CH_2OO (carbonyl oxide or the Criegee intermediate). 'FA···CI' is the complex of HC(=O)OH and CH_2OO. Formation of the complex 'FA···CI' is the most favourable path for HPMF decomposition at temperatures below 800 K.

anhydride and H_2O. They reported a 33.9 kcal mol^{-1} barrier to reaction ($\Delta H_0^{\ddagger}$). This is about 19.9 kcal mol^{-1} lower than the relative barrier height ($\Delta H_0^{\ddagger}$) for unimolecular decomposition of HPMF to formic acid anhydride and H_2O. Yet, this transition state is about 5.8 kcal mol^{-1} ($\Delta H_0^{\ddagger}$) higher than the endothermicity of the unimolecular decomposition of HPMF to carbonyl oxide and formic acid via the HC(=O)OH$\cdots$CH$_2$OO adduct [3]. Since our previous study [3], we have located a more favourable formic acid catalysed transition state leading to formic acid anhydride and H_2O, along with a H_2O-catalysed transition state leading to formic acid anhydride and H_2O. Figures 7(a) and (b) illustrate the transition states in which formic acid may catalyse HPMF to form H_2O and formic acid anhydride, according to Aplincourt and Ruiz-López (Figure 7(a)) and according to this work (Figure 7(b)), respectively. The transition state in Figure 7(b) is more favourable than that in Figure 7(a) by 14.5 kcal mol^{-1} ($\Delta H_0^{\ddagger} = 19.4$ kcal mol^{-1}). The reason for the more favourable HPMF + HC(=O)OH reaction through the transition state in Figure 7(b) may be the eight-membered ring transition state. The reaction through the transition state in Figure 7(a) has only a six-membered TS ring, and therefore may have more ring-strain than the transition state in Figure 7(b). Figure 7(c) illustrates the transition state through which H_2O may catalyse HPMF to form H_2O and formic acid anhydride. The transition state in Figure 7(c) is more favourable than that in Figure 7(a) by 11.7 kcal mol^{-1} ($\Delta H_0^{\ddagger} = 22.2$ kcal mol^{-1}).

The bimolecular decomposition of HPMF via an 'ancillary' species such as formic acid and H_2O may be very competitive with all the unimolecular decomposition routes discussed earlier. Except for the unimolecular decomposition of HPMF through an H-bonded adduct HC(=O)OH$\cdots$CH$_2$OO, all paths through the transition states depicted in Figures 7(a), (b), and (c) are more energetically favoured paths than unimolecular decomposition of HPMF. Compared to HPMF unimolecular decomposition through HC(=O)OH$\cdots$CH$_2$OO, only the paths through the transition states illustrated in Figures 7(b) and (c) are competitive. However, the true competitiveness of the bimolecular reactions through Figures 7(b) and (c) depends on the relative concentrations of formic acid and H_2O and thus the availability of these catalysing species in the reaction vessel. Bimolecular rate expressions for the catalysed decomposition of HPMF by HC(=O)OH and H_2O can be found in Table 5.

3.3. *Criegee intermediate reactions*

In our previous work [3], we found two HPMF decomposition paths leading to the formation of the Criegee intermediate (CI) of ethylene ozonolysis and formic acid. As mentioned above, the most favourable path involved a seven-membered ring transition state involving hydrogen transfer with C–O scission, which was endothermic by about 30 kcal mol^{-1} (to a CH$_2$OO$\cdots$HC(O)OH adduct) and virtually barrierless. With this strong possibility of CH$_2$OO being present in DME combustion, it is appropriate to consider reactions involving CH$_2$OO decomposition and bimolecular secondary reactions with molecules in the bath gas.

3.3.1. *Criegee intermediate unimolecular decomposition*

The Criegee intermediate, $\cdot$CH$_2$OO$\cdot$, formed in the unimolecular decomposition of HPMF, may itself

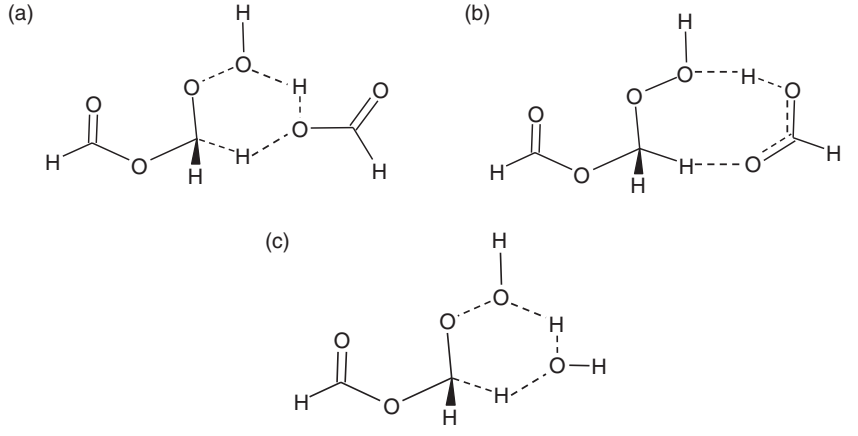

Figure 7. Schematic transition state structure of bimolecular decomposition of HPMF with (a) formic acid according to Aplincourt and Ruiz-López, [69] (b) formic acid according to this work, (c) H_2O according to this work.

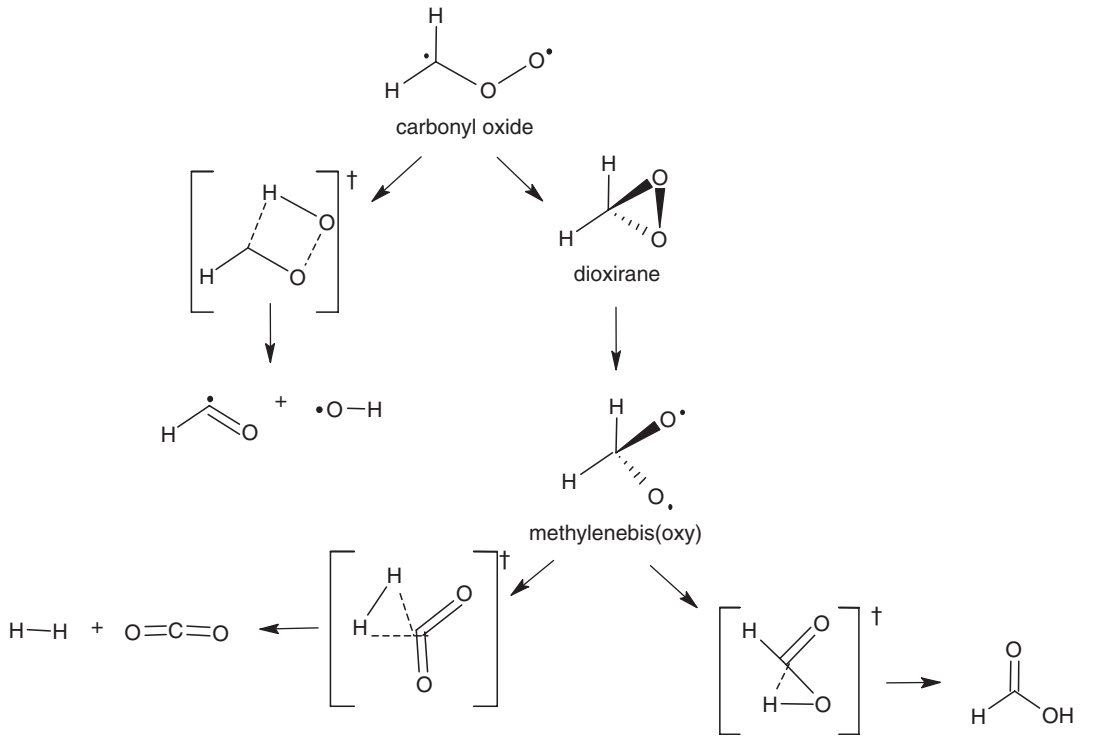

Figure 8. Reactions involved in the decomposition of the Criegee intermediate of ethylene ozonolysis.

undergo unimolecular decomposition, especially if it is vibrationally (or thermally) excited. Carbonyl oxide (CH_2OO) is believed to be formed vibrationally excited from combining O_3 and ethylene under atmospheric conditions. This vibrationally excited CH_2OO can undergo stabilisation via a bath gas or decompose/isomerise (much like $CH_3OCH_2OO\cdot$ and $\cdot CH_2OCH_2OOH$ formation discussed earlier). There are three main pathways postulated for carbonyl oxide isomerisation/decomposition. Two of these paths (isomerisation/decomposition via dioxirane rearrangement and decomposition to $H\dot{C}O$ and $\cdot OH$) are depicted in Figure 8. These paths were first postulated by Herron and Huie [70,71]. The third path is the scission of the O–O bond to form CH_2O and $O(^3P)$, which is very unlikely because of the energy needed to break this bond (47 kcal mol^{-1} according to CCSD(T)/TZ+2P calculations of Cremer *et al.* [72]). An intersystem triplet–singlet crossing has been suggested for this O–O bond scission process by Anglada *et al.* [73], which indicates that this may be an important reaction in photodissociation of CH_2OO but is likely not relevant to internal combustion.

Many theoretical studies have been devoted to the unimolecular rearrangement/decomposition of CH_2OO [14,15,43,72–80]. We have based our calculations of the two primary pathways (see Figure 8) on the most recent theoretical work of Cremer and coworkers [15,74]. From this work, we know that the barrier to formation of $H\dot{C}O$ and $\cdot OH$ (30.8 kcal mol^{-1}) [74] is less favourable than the cyclic rearrangement to form dioxirane (19.0 kcal mol^{-1}) [15]. However, $\cdot OH$ formation in ethylene ozonolysis has been detected experimentally [40–47]. The measured branching ratio for production of $\cdot OH$ under atmospheric conditions is about 12–40% [48]. However, internal combustion occurs at much higher temperatures and pressures. Thus it is not clear what energy state CH_2OO will be in when formed from HPMF decomposition at 1–40 atm pressures and 500–800 K temperatures.

Table 4 lists the rate expressions for the reactions involved in the decomposition/rearrangement of CH_2OO:

$$CH_2OO \rightarrow H\dot{C}O + \cdot OH, \qquad (28)$$

$$CH_2OO \rightarrow c - CH_2OO[\text{dioxirane}]. \qquad (29)$$

Our DFT-B3LYP activation energies $\Delta H^{\ddagger}_{298} = 32.6$ and 21.1 kcal mol^{-1} for reactions (28) and (29), respectively, are consistent with those calculated with CCSD(T) by Cremer and coworkers [15,74]. Clearly, from energetics alone, reaction (29) is much more favourable than reaction (28). If CH_2OO is formed vibrationally excited, reaction (28) may be a viable

path leading to ·OH formation, but further study of the carbonyl oxide under diesel engine conditions with master equation analysis similar to those of Olzmann *et al.* [14] and Kroll *et al.* [81] under atmospheric conditions may be useful.

Dioxirane can then undergo O–O scission to produce the methylenebis(oxy) biradical:

$$c-CH_2OO \rightarrow \cdot OCH_2O \cdot \quad \text{[methylenebis(oxy)]}. \quad (30)$$

The barrier to reaction is $\Delta H^{\ddagger}_{298} = 19.0\,\text{kcal mol}^{-1}$ according to our DFT-B3LYP//6-311G** calculations. This is in good agreement with the $\Delta H^{\ddagger}_{298} = 19.6\,\text{kcal mol}^{-1}$ (B3LYP/6-311+G(3df,3pd)) and $18.0\,\text{kcal mol}^{-1}$ (MR-AQCC/6-311G(3df,3pd)) calculations of Cremer *et al.* [15]. Methylenebis(oxy) has two competitive paths to reaction:

$$\cdot OCH_2O \cdot \rightarrow HC(=O)OH, \quad (31)$$

$$\cdot OCH_2O \cdot \rightarrow CO_2 + H_2. \quad (32)$$

The isomerisation and dissociation barriers of reactions (31) and (32), respectively, are both very small: $\Delta H^{\ddagger}_{298} = 2.7$ and $1.2\,\text{kcal mol}^{-1}$, respectively. These values are essentially the same, considering that DFT-B3LYP has an average error of ~3–4 kcal mol^{-1}. These results are consistent with DFT-B3LYP/6-311+G(3df,3pd) results of Cremer *et al.* ($\Delta H^{\ddagger}_{298} = 2.1$ and $0.2\,\text{kcal mol}^{-1}$ for reactions (31) and (32)) [15]. However, the CCSD(T)/cc-pVTZ2P+f,d energy results slightly emphasise that reaction (31) may be more favourable than reaction (32) ($\Delta H^{\ddagger}_{298} = 1.8$ and $2.4\,\text{kcal mol}^{-1}$, respectively), but, again, the difference is extremely slight. Reaction (31)'s A_∞ is slightly higher than that of reaction (32) at 298 K ($A_\infty = 2.66 \times 10^{13}$ and $1.10 \times 10^{13}\,\text{s}^{-1}$, respectively) and 600 K ($A_\infty = 2.87 \times 10^{13}$ and $1.39 \times 10^{13}\,\text{s}^{-1}$, respectively). However, the A_∞ of reaction (32) grows faster than that of reaction (31) with temperature. Thus, the gap between k_∞ for reaction (31) ($1.98 \times 10^{11}\,\text{s}^{-1}$) and k_∞ for reaction (32) ($1.45 \times 10^{12}\,\text{s}^{-1}$) is larger at 298 K than it is at 600 K (k_∞ for reaction (32) is $2.52 \times 10^{12}\,\text{s}^{-1}$, and k_∞ for reaction (32) is $5.07 \times 10^{12}\,\text{s}^{-1}$ at 600 K).

Formic acid produced via reaction (31) may also decompose further:

$$HC(=O)OH \rightarrow CO + H_2O, \quad (33)$$

$$HC(=O)OH \rightarrow CO_2 + H_2. \quad (34)$$

The DFT-B3LYP barrier for reaction (33) is $\Delta H^{\ddagger}_{298} = 67.6\,\text{kcal mol}^{-1}$. This agrees well with the $\Delta H^{\ddagger}_{298} = 69.6\,\text{kcal mol}^{-1}$ result (CCSD(T)/6-311+G(3df,3pd)) calculated by Cremer *et al.* [15]. The barrier for reaction (34) is almost the same height as reaction (33): $\Delta H^{\ddagger}_{298} = 67.1\,\text{kcal mol}^{-1}$ (from the lowest energy configuration of formic acid). This is consistent with the $\Delta H^{\ddagger}_{298} = 69.6\,\text{kcal mol}^{-1}$ ((CCSD(T)/6-311+G(3df, 3pd)) result calculated by Cremer *et al.* [15] (from the lowest energy configuration of formic acid). A summary of all reaction rate constants is given in Table 4.

3.3.2. *Possible Criegee intermediate bimolecular reactions*

A Criegee intermediate stabilised via collisions could be involved in bimolecular reactions with ambient bath molecules. It is known that a stabilised Criegee intermediate can react with ambient H_2O [50,51,53,54], $H_2C{=}O$ and other carbonyl compounds [40–42], $HC(=O)OH$ [40,49,52,54,82], SO_2 [40,83], NO [84], NO_2 [84], CO [40], and CO_2 [40]. Theoretical calculations on a subset of these possible bimolecular reactions (CH_2OO with H_2O, $H_2C{=}O$, $HC(=O)OH$, SO_2, and CO_2) have been done only recently. [3,14,16,69,85–87] These studies indicate that the CH_2OO is most likely to react with H_2O, $H_2C{=}O$, and $HC(=O)OH$ because of relatively low barriers to addition. Figure 9 depicts proposed mechanisms for the bimolecular reactions of CH_2OO with H_2O, $H_2C{=}O$, and $HC(=O)OH$. We have already described the reactions of CH_2OO and $HC(=O)OH$ indirectly in considering the decomposition of HPMF, which is the product of CH_2OO and $HC(=O)OH$ combination. Thus we will not describe these reactions here. Although bimolecular reactions involving NO and methyl formate ($CH_3OC(=O)H$) may be important in DME combustion chemistry (as indicated in the experimental work of Liu *et al.* [8]) these additions to the mechanism will have to await future work.

According to the recent electronic structure work of Alplincourt and Ruiz-López [16,69], the additions of H_2O and $H_2C{=}O$ to CH_2OO are the most important routes to CH_2OO reaction. The reactions are depicted in Figure 9. For H_2O, Aplincourt and Ruiz-López [16] based their calculations on the mechanism put forth by Hatakeyama *et al.* [51]. In their near-UV photolysis of ketene and diazomethane in the presence of [18]O-labeled H_2O, Hatakeyama *et al.* [51] observed that $HC(={}^{18}O)OH$, $HC(=O)^{18}OH$, and unlabeled H_2O were formed. Rapid proton exchange between formic acid and water was suggested to be responsible for the carbonyl-labeled and hydroxyl-labeled versions of formic acid. Aplincourt and Ruiz-López [16] found a van der Waals complex for $H_2O\cdots CH_2OO$, which undergoes a concerted transfer of hydrogen from H_2O to the terminal oxygen of CH_2OO with the remaining

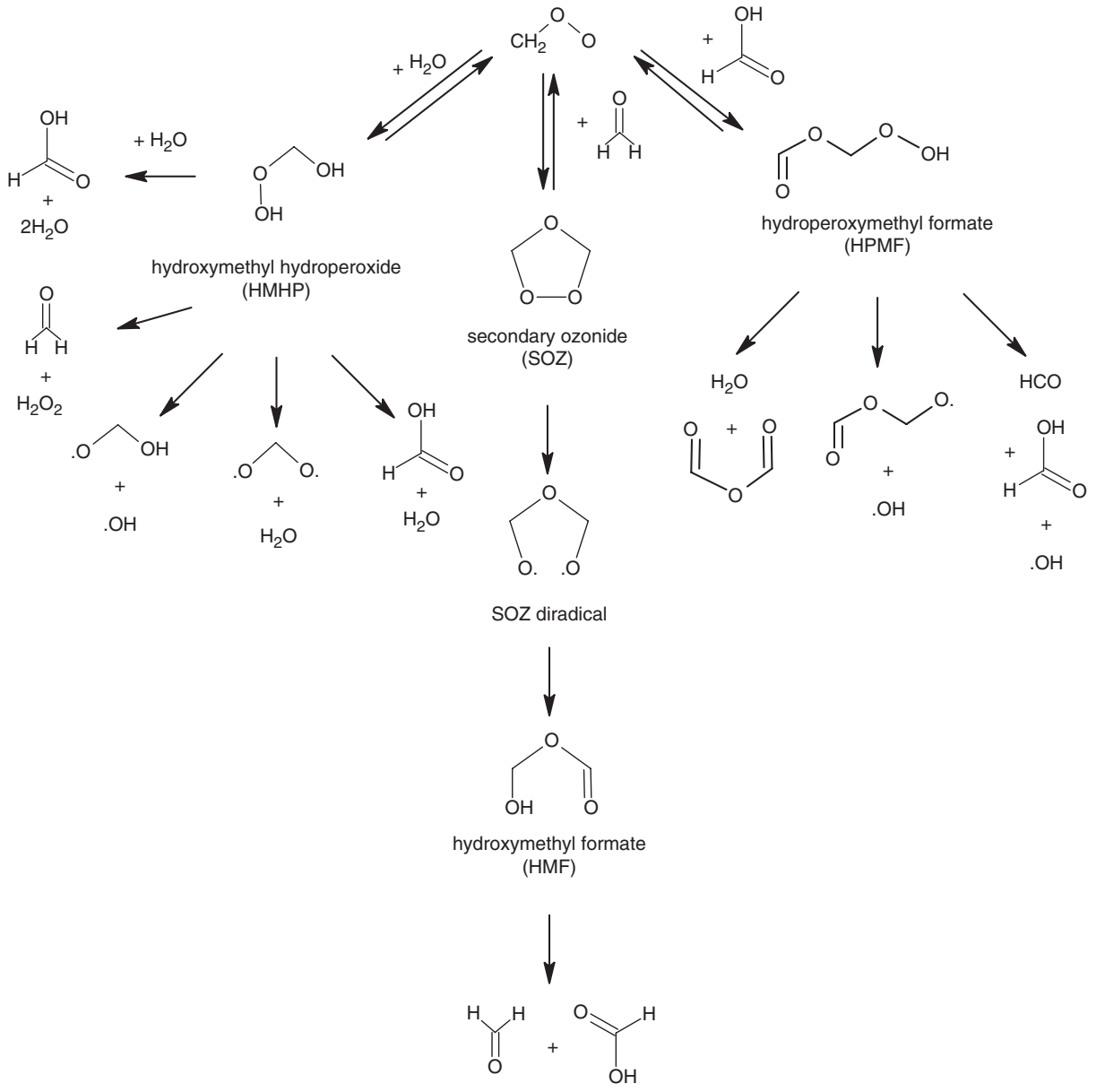

Figure 9. Selected bimolecular reactions of the Criegee intermediate.

·OH bonding to the radical carbon site of CH_2OO to form a C–O bond. Thus, the resulting compound is hydroxymethyl hydroperoxide, $HOCH_2OOH$ (HMHP). Aplincourt and Ruiz-López [16] could not find a transition state leading to unimolecular decomposition of HMHP into H_2O and formic acid. Instead, they found a transition state in which a second H_2O serves as a catalyst to decompose HMHP into H_2O and HC(=O)OH. More recently, Crehuet *et al.* [85] and Hasson *et al.* [87] considered other avenues of HMHP decomposition, including O–O scission to produce hydroxymethoxy radical ($\cdot OCH_2OH$) and ·OH, and decomposition to H_2O_2 and $H_2C{=}O$, in their quantum chemical calculations. Crehuet *et al.* [85] did find transition states for the unimolecular decomposition of HMHP into H_2O and HC(=O)OH, but found that the H_2O-assisted decomposition was more favourable energetically. O–O scission was shown to be the most energetically favourable of all $CH_2OO + H_2O$ processes. Kinetically, O–O scission is also the most favourable unimolecular decomposition pathway because the A_∞-factors for simple scission reactions tend to be larger than any class of reaction involving tight transition states [22,87]. O–O scission may aid in

Table 5. High-pressure rate expressions for secondary chemistry of intermediates found in gas-phase ozonolysis of ethylene in terms of Equation (4). Note that rate coefficients are in s^{-1} for unimolecular reactions or in $cm^3\,mol^{-1}\,s^{-1}$ for bimolecular reactions. These reactions are shown in Figure 9. SOZ stands for secondary ozonide (see Figure 9 for the chemical structure). All rate coefficients have been calculated with KHIMERA unless noted otherwise. Activation energies are in kcal mol^{-1}.

Reaction	k_∞	k_∞(600 K)
Bimolecular decomposition of HPMF		
$HOOCH_2OC(=O)H + H_2O \rightarrow 2H_2O + HC(=O)OH$	$1.62T^{3.70}e^{-20.1/RT}$	1.47×10^3
$HOOCH_2OC(=O)H + HC(=O)OH \rightarrow 2HC(=O)OH + H_2O$	$1.01 \times 10^{-2}T^{3.78}e^{-17.7/RT}$	1.14×10^2
Bimolecular reactions of CH_2OO		
Addition to $H_2C=O$		
$SOZ \rightarrow CH_2OO + H_2C=O$	$5.08 \times 10^{13}T^{0.96}e^{-42.6/RT}$	7.37
$SOZ \rightarrow$ SOZ-diradical	$4.45 \times 10^{11}T^{0.64}e^{-18.9/RT}$	3.49×10^6
SOZ-diradical $\rightarrow HOCH_2OC(=O)H$	$2.94 \times 10^{11}T^{0.38}e^{-4.6/RT}$	7.06×10^{10}
$HOCH_2OC(=O)H \rightarrow HC(=O)OH + H_2C=O$	$2.94 \times 10^{11}T^{0.51}e^{-16.6/RT}$	6.90×10^6
Addition to H_2O		
$HOOCH_2OH \rightarrow CH_2OO + H_2O$	$3.09 \times 10^{11}T^{0.35}e^{-42.2/RT}$	1.23×10^{-3}
$HOOCH_2OH + H2O \rightarrow 2H_2O + HC(=O)OH$	$6.25 \times 10^{-1}T^{3.57}e^{-21.6/RT}$	7.02×10^1
$HOOCH_2OH \rightarrow \cdot OH + \cdot OCH_2OH$[a]	$5.63 \times 10^{20}T^{-1.31}e^{-37.6/RT}$	2.60×10^3

[a]VRRKM rate expression calculated with VARIFLEX. Varshni parameters for the potential are $D_e = 14{,}772\,cm^{-1}$, $\beta = 0.662\,Å^{-2}$, and $R_e = 1.413\,Å$.

DME chain branching because of its production of an ·OH.

For the reaction of $H_2C{=}O$ and CH_2OO, the formation of the well-known secondary ozonide (SOZ), an intermediate postulated in the ozonolysis of ethylene [88–90], is the most likely path (see Figure 9). The first step in the postulated mechanism of SOZ decomposition to formic acid is scission of the O–O bond to form a diradical [88–90]. This diradical then may undergo a hydrogen-transfer isomerisation to form a fairly stable intermediate, hydroxymethyl formate (HMF) [88–90]. which is observed experimentally [41]. The mechanism for the decomposition of HMF to formic acid was postulated by Aplincourt and Ruiz-López [16]. This involves another hydrogen transfer, where the hydroxyl hydrogen transfers to the carbonyl oxygen with a concerted C–O scission. While Aplincourt and Ruiz-López have explored other avenues for the addition of $H_2C{=}O$ to CH_2OO, the $H_2C{=}O$-catalysed rearrangement of CH_2OO depicted in Figure 9 has the lowest barrier to reaction overall (without the involvement of photo-excited species such as $O_2(^1\Delta_g)$).

A summary of the unimolecular and bimolecular reactions for H_2O and $H_2C{=}O$ addition to CH_2OO (Figure 9) considered in this work are listed in Table 5. Note that, where possible, a reaction is written as a unimolecular reaction rather than an association reaction. In the global kinetics modeling (to be discussed shortly), the reverse reactions are automatically calculated via microscopic reversibility.

3.4. *Multiwell stochastic master equation calculations*

As mentioned earlier in Section 3.1, Sehested *et al.* [6] proposed a Lindemann-type mechanism where reaction (6) produces a chemically activated peroxy radical ($CH_3OCH_2OO{\cdot}^*$). The vibrationally excited peroxy radical can either decompose back to $CH_3O\dot{C}H_2 + O_2$, stabilise via bath gas collisions, or rearrange and decompose into product species ($H_2C{=}O$ and ·OH). This mechanism can be modeled using a multiple-well (potential well) master equation method. Here we used the stochastic multiple-well master equation method as implemented in MultiWell [31,32] to model the chemical activation of $CH_3OCH_2OO{\cdot}$ from $CH_3O\dot{C}H_2 + O_2$ combination and subsequent stabilisation and/or dissociation to products and $CH_3O\dot{C}H_2 + O_2$. The chain propagation pathway has two potential wells, $CH_3OCH_2OO{\cdot}$ and $\cdot CH_2OCH_2OOH$, and two exit channels, $CH_3O\dot{C}H_2 + O_2$ and $2H_2C{=}O + \cdot OH$. The estimated Lennard–Jones parameters [27] from T_c, V_c, and P_c for CH_3OCH_2OOH ($\epsilon/k_B = 421$ K and $\sigma = 6.02$ Å) were assumed for both radical intermediates $CH_3OCH_2OO{\cdot}$ and $\cdot CH_2OCH_2OOH$. O_2 rather than N_2 was used to model the collision gas, since the primary diluent of the experiments of Sehested *et al.* [6] was O_2. The potential well depth of $CH_3OCH_2OO{\cdot}$ with respect to the $CH_3O\dot{C}H_2 + O_2$ was adjusted to reflect the $\Delta H_0 = 35.0$ kcal mol^{-1} of reaction (6) implied by the thermochemical estimations made by Curran *et al.* [4,5]. The microcanonical rate of reaction (6) was estimated

using the inverse Laplace transform method [21] as implemented in MultiWell. We estimated A_∞ for the reverse of reaction (6) via detailed balance from the partition functions of $CH_3OCH_2OO\cdot$, $CH_3O\dot{C}H_2$, and O_2 and the high-pressure rate expression at 296 K reported by Sehested *et al.* [7] ($7.53 \times 10^{12}\,cm^3\,mol^{-1}$) for the forward reaction of (6) (which is more accurate than our predicted rates). We obtain $A_\infty = 9.08 \times 10^{15}\,s^{-1}$ for the reverse of reaction (6), derived from detailed balance of the A_∞ factor of Sehested *et al.*, which is close to the range typical for simple scission reactions [22]. The density of states for $CH_3OCH_2OO\cdot$, $\cdot CH_2OCH_2OOH$, and the transition states for isomerisation and disproportionation reactions (7) and (7) were calculated from their respective vibrational frequencies and moments of inertia computed previously [2]. In the simulation, the dissociation to $CH_3O\dot{C}H_2 + O_2$ is treated as an exit channel where $CH_3O\dot{C}H_2$ is not allowed to recombine with O_2. However, all the $CH_3O\dot{C}H_2$ is expected to react in the physical system. Thus the final mole fractions of stabilised $CH_3OCH_2OO\cdot$, $\cdot CH_2OCH_2OOH$, and $2H_2C{=}O + \cdot OH$ were normalised to reflect complete consumption of $CH_3O\dot{C}H_2$.

Figure 10 shows the percent yields of our model compared with the experimental results of Sehested *et al.* [6] and Jenkin *et al.* [38]. Using the DFT-B3LYP barriers for reactions (7) and (8), we observe that our model (gray solid line) overestimates the production of formaldehyde and ·OH with increasing pressure. To ameliorate the over-production of formaldehyde and ·OH, we either artificially increase the barrier height of reaction (7) or the barrier height of reaction (8). This is reasonable, since DFT-B3LYP generally underestimates barrier heights. First, we increase the barrier height of reaction (7) by $3\,kcal\,mol^{-1}$. With this adjustment, we see in Figure 10 (solid black line) much improved agreement between our model and the experimental $CH_2O/2$ product yield. This suggests the DFT-B3LYP activation energy of reaction (7) is very likely $3.0\,kcal\,mol^{-1}$ too small.

We also show the stabilisation of the $CH_3OCH_2OO\cdot$ in Figure 10. With the stabilisation of $CH_3OCH_2OO\cdot$ at higher pressures, $CH_3OCH_2OO\cdot$ undergoes self-reactions. These self-reactions lead to formation of methyl formate ($CH_3OC(=O)H$) and CH_3OCH_2OOH. Unfortunately, we cannot include these self-reactions in the model, but the presence of stabilised $CH_3OCH_2OO\cdot$ in the model suggests the opportunity for self-reactions to occur. By contrast, $\cdot CH_2OCH_2OOH$ does not stabilise at these pressures and 296 K in our model. This is because the rate of reaction (8) is very favourable and does not allow any stabilisation of $\cdot CH_2OCH_2OOH$. This provides further

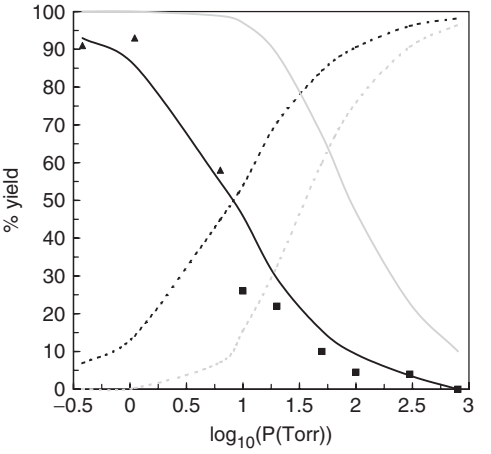

Figure 10. Formaldehyde production of low-pressure DME oxidation at 296 K as a function of pressure. (▲) Experimental data of Sehested *et al.* [6]; (■) experimental data of Jenkin *et al.* [38]; (gray solid line) $2CH_2{=}O + \cdot OH$ formation in model using DFT-B3LYP activation barriers; (gray dashed line) predicted $CH_3OCH_2OO\cdot$ stabilisation; (black solid line) $2CH_2{=}O + \cdot OH$ formation with a $3.0\,kcal\,mol^{-1}$ increase of reaction (7)'s barrier; (black dashed line) $CH_3OCH_2OO\cdot$ stabilisation with a $3.0\,kcal\,mol^{-1}$ increase of reaction (7)'s barrier. Note that the black lines can be reproduced if the barrier to reaction (8) is increased by $6.0\,kcal\,mol^{-1}$. Either way, the DFT-B3LYP method is known to underestimate reaction barriers, so this empirical increase is justified.

justification for Sehested *et al.*'s [6] neglect of the role of $\cdot CH_2OCH_2OOH$ in forming formaldehyde and ·OH in modeling their data. In contrast, the model of Yamada *et al.* [10] greatly underestimates the barrier of reaction (7) and overestimates the barrier of reaction (8). Thus their model would possibly show some stabilisation of $\cdot CH_2OCH_2OOH$ at the conditions considered here.

However, the lack of stabilised $\cdot CH_2OCH_2OOH$ in our master equation simulation may contradict Liu *et al.*'s [8] measurements. They observed the formation of formic acid in their flow-reactor/FTIR work. Formic acid is most likely formed via chain-branching (reactions of which will be discussed in the next section), which requires some stabilisation of $\cdot CH_2OCH_2OOH$ in order to facilitate reaction with O_2. If the barrier height of reaction (7) is held at our DFT-B3LYP value, and the barrier height of reaction (8) is artificially increased by $6.0\,kcal\,mol^{-1}$, then we find almost exactly the same quantitative agreement with the work of Sehested *et al.* [6] and Jenkin *et al.* [38]. A very small amount (~0.4%) of $\cdot CH_2OCH_2OOH$ stabilises close to 1 atm in our model, which can lead to chain branching and formic

acid formation (if conditions are conducive). This suggests that the combination of the two reaction barriers of reactions (7) and (8) should be viewed as an *effective* barrier to total reaction to formaldehyde and ·OH.

At higher temperatures and pressures, the stabilisation of $\cdot CH_2OCH_2OOH$ is expected to be more pronounced, because of its role as a precursor in chain-branching. However, the multi-well master equation method here is limited to modeling a series of unimolecular reactions. A more flexible modeling method is needed to include bimolecular reactions such as that of O_2 and the $\cdot CH_2OCH_2OOH$ branching precursor. A perfectly stirred reactor simulation is one such method, which will be addressed next.

3.5. *Perfectly stirred reactor calculations*

The objective of these global kinetics simulations is to test the first-principles-derived rate expressions discussed here in a large-scale model that may be more easily compared to experimental data. Here we have modified and extended the mechanism of Curran *et al.* [4,5]. Extensions include modified Arrhenius expressions fits at 10 atm for the existing and additional unimolecular and recombination reactions mentioned in this work (for which Curran and coworkers estimated high-pressure limit rate constants). Extensions include adding HPMF decomposition paths other than O–O scission, as well as Criegee intermediate unimolecular and bimolecular reactions, to the original mechanism of Fischer *et al.* The primary focus is on the lowest temperature regime (550–700 K) where chain-branching is responsible for first-stage autoignition of dimethyl ether. Modeling of second-stage autoignition via O–O scission in peroxide species such as HOOH in the intermediate temperature regime (700–1000 K) is important, but beyond the scope of this work.

3.5.1. *Comments regarding relative heats of formations*

To be consistent with the thermochemistry of the mechanism of Fischer *et al.*, certain adjustments to our DFT-B3LYP heats of formation had to be made. The largest discrepancy in the heats of formation can be attributed to the reactions in which molecular O_2 is added to a radical species (reaction (6) and reaction (12)) where the multi-reference character is not well-captured by the DFT-B3LYP level of theory used in these calculations. We have used group additivity estimates of the $\Delta H_f^\circ(298\,K)$'s for $CH_3O\dot{C}H_2$, $CH_3OCH_2OO\cdot$, $\cdot CH_2OCH_2OOH$, and $\cdot OOCH_2OCH_2OOH$ (species involved in reactions (6) and (12)) from Curran *et al.* [4,5] to estimate corrections in the $\Delta H_f^\circ(298\,K)$'s of our previous energetics results [2,3]. The experimental $\Delta H_f^\circ(298\,K)$ of ·OH ($\Delta H_f^\circ(298\,K) = 9.3\,kcal\,mol^{-1}$) [91,92] was used, along with relative heats of reaction from previous DFT-B3LYP//6-311G** calculations [2,3], to derive $\Delta H_f^\circ(298\,K)$ for HPMF and $\cdot OCH_2OC(=O)H$. Table 6 lists our $\Delta H_f^\circ(298\,K)$'s relative to Curran *et al.*'s estimate [4,5] of the $\Delta H_f^\circ(298\,K)$ of $CH_3O\dot{C}H_2$ in the second column. The fifth column lists the adjustment to the second column based on the estimated heats of reactions implied by Curran *et al.*'s $\Delta H_f^\circ(298\,K)$'s for the species involved in reactions (6) and (12). The fairly good agreement between the third through sixth values in the fourth and fifth columns of Table 6 shows that O_2 addition reactions cause the greatest discrepancy between our results and those of Curran *et al.* [4,5].

For the species involved in the unimolecular decomposition/isomerisation of carbonyl oxide (CH_2OO), ΔH_f° (298 K)'s were estimated by shifting the energetics of the rearrangement of CH_2OO to formic acid to take into account formic acid's experimental $\Delta H_f^\circ(298\,K)$ of $-90.5\,kcal\,mol^{-1}$ [91,93]. According to the mechanism for CH_2OO isomerisation to formic acid [15], dioxirane and methylenebis(oxy) are short-lived intermediates on the way to formic acid or decomposition to CO_2 and H_2 (see Figure 8). Thus $\Delta H_f^\circ(298\,K)$'s for dioxirane and methylenebis(oxy) were also estimated based on the experimental $\Delta H_f^\circ(298\,K)$ for formic acid and the DFT-B3LYP//6-311G** relative enthalpies performed in this work [91,93]. The estimated $\Delta H_f^\circ(298\,K)$'s appear in Table 6. Cremer *et al.* [15] performed an in-depth study of the unimolecular reactions of CH_2OO to stable products using DFT-B3LYP/6-311+G(3df,3pd) to calculate geometries with an additional CCSD(T) or MR-AQCC/6-311+G(3df,3pd) single-point energy calculation with the DFT-B3LYP optimised geometries. Their $\Delta H_f^\circ(298\,K)$'s for carbonyl oxide, dioxirane, and methylenebis(oxy) also appear in Table 6. Our $\Delta H_f^\circ(298\,K)$ for carbonyl oxide is a couple of $kcal\,mol^{-1}$ lower, while our $\Delta H_f^\circ(298\,K)$ for dioxirane and methylenebis(oxy) are a few $kcal\,mol^{-1}$ higher, than those of Cremer *et al.* [15], which is within the error of the DFT-B3LYP level of theory used in this work ($\sim$3–4 $kcal\,mol^{-1}$). We also used the NIST group additivity estimator [94] to estimate $\Delta H_f^\circ(298\,K)$ for dioxirane. However, the value is much higher than $\Delta H_f^\circ(298\,K)$ of dioxirane derived by us and by Cremer *et al.* [15]. This group additivity estimate seems unphysical, since dioxirane is the only one of these three intermediates of ethylene ozonolysis that has

Table 6. Comparison of ΔH°_f's at 298 K in kcal mol^{-1} for selected species involved in DME low-temperature autoignition.

	ΔH°_f				
Species	(this work[a])	(expt.)	(GA)	(adjusted[b])	(other theory)
$CH_3O\dot{C}H_2$	1.0[c]		1.0[d]	1.0[c]	0.1[e]
$CH_3OCH_2OO\cdot$	−29.3		−34.6[d]	−34.6	−33.9[e]
$\cdot CH_2OCH_2OOH$	−15.2		−24.0[d]	−21.5	−26.5[5]
$\cdot OOCH_2OCH_2OOH$	−45.8		−59.6[d]	−57.1	
$HOOCH_2OC(=O)H$ (HPMF)	−93.0		−109.4[d]	−106.3	
$\cdot OCH_2OC(=O)H$	−60.3		−75.5[d]	−73.7	
$HC(=O)OH$		−90.5[f]	−90.2[d]		
CH_2OO	−24.7[g]				27.0[h]
Dioxirane	2.8[g]		27.6[i]		−0.3[j]
Methylenebis(oxy)	4.3[g]				0.9[j]
$HC(=O)OC(=O)H$	−116.1[k]		−110.7[i]		
$HOOCH_2OH$ (HMHP)	−77.1[l]		−74.8[i]		
Secondary ozonide (SOZ)	−49.4[m]				
SOZ-diradical	−34.9[m]				
$HOCH_2OC(=O)H$ (HMF)	−127.0[m]		−129.2[i]		
$\cdot OH$		9.3[n]			
H_2O		−57.8[n]			
CO		−26.4[n]			
CO_2		−94.1[n]			
$CH_2=O$		−27.7[n]			
$H\dot{C}O$		10.4[n]			

[a]DFT-B3LYP//6-311G** from this and previous work [2,3].
[b]Adjustments to the ΔH°_f's at 298 K estimated in this work made to reactions (6) and (12) to reflect ΔH°_f's of $CH_3OCH_2OO\cdot$ and $\cdot OOCH_2OCH_2OOH$ estimated by Curran *et al.* [4,5].
[c]ΔH°_f from Curran *et al.* [4,5] assumed for this work.
[d]ΔH°_f from Curran *et al.* [4,5]
[e]ΔH°_f derived by Yamada *et al.* [10] using CBS-q/MP2//6-31G(d,p) isodesmic reactions [10].
[f]ΔH°_f from the NIST Chemistry Webbook database [91], which cites the work of Guthrie [93].
[g]ΔH°_f derived from DFT-B3LYP//6-311G** for the CH_2OO decomposition to formic acid (this work), using the experimental ΔH°_f of formic acid (from the NIST Chemistry Webbook database [91,93]) as a baseline.
[h]ΔH°_f derived by Cremer *et al.* [15] using CCSD(T)//TZ2P energies with B3LYP//6-311+G(3df,3pd) zero point energies and temperature corrections and using the experimental ΔH°_f of -90.6 kcal mol^{-1} [97].
[i]ΔH°_f estimated using the NIST group additivity estimator [94].
[j]ΔH°_f derived by Cremer *et al.* [95] using MR-AQCC/6-311+G(3df,3pd) energies with B3LYP//6-311+G(3df,3pd) zero point energies and temperature corrections and using the experimental ΔH°_f of -90.6 kcal mol^{-1} [97].
[k]ΔH°_f derived from DFT-B3LYP//6-311G** for formic acid anhydride (from previous work [93]) dissociating to CO and H_2O. Experimental ΔH°_f for CO and H_2O [91,92] in conjunction with heat of reaction of Equation (27).
[l]ΔH°_f derived from DFT-B3LYP//6-311G** heat of formation and experimental ΔH°_f for H_2O [91,92] and ΔH°_f of CH_2OO derived here.
[m]ΔH°_f derived from DFT-B3LYP//6-311G** heat of formation and experimental ΔH°_f for $CH_2=O$ [91,92] and ΔH°_f of CH_2OO derived here.
[n]Experimental ΔH°_f from the NIST Chemistry Webbook database [91], which cites the review of Chase [92].

enough thermodynamic stability to be detected spectroscopically [95].

Heats of formation for intermediates involved in the bimolecular reactions of $\cdot CH_2OO\cdot$ with $H_2C{=}O$, CO_2, and H_2O were estimated from $\Delta H^\circ_f(298\,K)$ of $\cdot CH_2OO\cdot$ determined above, experimental $\Delta H^\circ_f(298\,K)$'s of the respective second species, and the respective DFT-B3LYP heats of reactions. The $\Delta H^\circ_f(298\,K)$'s for HMHP and HMF are in good agreement with group additivity values estimated using the NIST Webbook group additivity estimator [94]. The $\Delta H^\circ_f(298\,K)$'s for these intermediates appear in Table 6.

Formic acid anhydride's $\Delta H^\circ_f(298\,K)$ was estimated using the experimental literature values of CO ($\Delta H^\circ_f(298\,K) = -26.4$ kcal mol^{-1}) [91,92] and formic acid ($\Delta H^\circ_f(298\,K) = -90.5$ kcal mol^{-1}) [91,93]. These species are the products of reaction (27). The DFT-B3LYP heat of reaction (27) is $\Delta H^\circ_f(298\,K) = -0.8$ kcal mol^{-1}. Thus DFT-B3LYP $\Delta H^\circ_f(298\,K)$ for formic acid anhydride is -116.1 kcal mol^{-1}. This is about 5 kcal mol^{-1} lower

than the group-additivity value of $-110.7\,\mathrm{kcal\,mol^{-1}}$ calculated with the NIST Webbook group additivity estimator [94].

3.5.2. *PSR modeling results and comparison with experiment and previous modeling efforts*

In sensitivity analyses, Curran *et al.* [5] have noted that their PSR modeling was most sensitive to reactions (8) and (12) (both reactions involve $\cdot CH_2OCH_2OOH$) and the abstraction of a hydrogen from CH_3OCH_3 by the highly reactive ·OH radicals at 593 K (temperature of peak first-stage chain-branching). With reactions (8) and (12), we have shown that our reaction rate constants are higher than those used by Curran *et al.* [4,5] in their modeling. Thus, we see profound changes in product yields in our modeling efforts compared with those of Curran *et al.* due to differences between our rate constants and those used by Curran *et al.* for reactions (8) and (12) alone. Here we used our 10 atm results for reactions (8) (with a $6.0\,\mathrm{kcal\,mol^{-1}}$ increase in the reaction barrier) and (12). The model is also extremely sensitive to the underlying thermochemistry in this part of the mechanism. The $\Delta H_f^\circ(298\,\mathrm{K})$ for $\cdot CH_2OCH_2OOH$ from the group additivity method of Curran *et al.* [4,5] seems to yield results more in sync with experiment than our adjusted DFT-B3LYP $\Delta H_f^\circ(298\,\mathrm{K})$ (see Table 6). Using our $\Delta H_f^\circ(298\,\mathrm{K})$, $\cdot CH_2OCH_2OOH$ appears to be too unstable, and no branching products occur in the 550–700 K temperature regime. This implies that the underlying DFT-B3LYP thermochemistry is inadequate and there is a need for more accurate electronic structure calculations. Because of this, we chose to use the $\Delta H_f^\circ(298\,\mathrm{K})$'s estimated using group additivity from Curran *et al.*'s work [4,5].

Another area of the mechanism that shows great differences between our modeling efforts and those of Curran *et al.* is in the decomposition of $\cdot OCH_2OC(=O)H$ (formed from O–O scission of HPMF). As mentioned previously, Curran *et al.* [5] proposed a circuitous pathway for decomposition of $\cdot OCH_2OC(=O)H$ (reactions (17), (18), (19), and (20)), but Liu *et al.* [8] proposed a one-step decomposition (reaction (21)), which we determined to have a much lower barrier than that of reaction (17). Since the $H\dot{C}O$ readily undergoes hydrogen abstraction to form CO, the yield in CO increased dramatically in our modeling efforts compared with the efforts of Curran *et al.* (see reaction (21)). Curran *et al.* estimated that reactions (18) and (19) have equal barrier heights (with reaction (19) being exothermic and thus more thermodynamically likely). Thus, the production of CO_2 is competitive with the production of CO in their model. Since the predicted CO mole fraction in Curran *et al.*'s modeling efforts is much greater than that of experiment [36] for the stoichiometric case and slightly higher than experiment for the fuel lean case ($\phi = 0.2$), the increased CO in our modeling efforts via reaction (21) overestimates the CO yield even more. However, we have shown in our analysis of the unimolecular decomposition of HPMF that CH_2OO production is very competitive with O–O scission. We have shown that the most likely unimolecular path for CH_2OO is through reactions (29), (30), and (32) at the temperatures of interest here. Thus, the production of CO_2 is competitive with the production of CO in our modeling work. Our model does not seem to be sensitive to secondary chemistry involving bimolecular HPMF decomposition, but is sensitive to the bimolecular reaction of $H_2C{=}O$ addition to CH_2OO to produce the secondary ozonide (SOZ, see Figure 9 for structure). SOZ undergoes rearrangement that eventually leads to the formation of $H_2C{=}O$ and $HC(=O)OH$, as shown in Figure 9. Thus unimolecular HPMF and CH_2OO decomposition pathways and $H_2C{=}O$-catalysed conversion of CH_2OO to $HC(=O)OH$ seem to be dominant in the low-temperature regime (550–700 K).

Figures 11(a) and (b) show our results for a stoichiometric (one mole of DME to three moles of O_2 for complete combustion to H_2O and CO_2) equivalence ratio (ϕ) of 1.0 and a fuel lean (oxygen in excess) equivalence ratio (ϕ) of 0.2, respectively. Though Dagaut *et al.* [36] did not detect $HC(=O)OH$ in their apparatus, $HC(=O)OH$ is a major low-temperature (550–700 K) product observed by both Liu *et al.* [8] and Curran *et al.* [5]. Thus, we show our predicted $HC(=O)OH$ yields in Figures 11(a) and (b). In both cases, we see qualitative agreement with experiment, but the predicted mole fractions of major products (CO, CO_2, and $H_2C{=}O$) are too low. In the fuel-lean case, it seems that peak production of 550–700 K chain-branching products in the model is shifted to lower temperatures (see Figure 11(b)). The predicted $HC(=O)OH$ yield in our modeling efforts is higher than our predicted CO yield for $\phi = 1.0$ (see Figure 11(a)), which is contrary to Curran *et al.*'s [5] predicted relative yields. For $\phi = 0.2$, the predicted $HC(=O)OH$ yield is lower than the predicted CO yield, in accord with Curran *et al.*'s results, but our predicted $HC(=O)OH$ yield is closer to the predicted CO yield than it is for Curran *et al.* (see Figure 11(b)). The higher relative predicted $HC(=O)OH$ yield seen in our modeling efforts is due to the addition of many favourable avenues to $HC(=O)OH$ production (e.g., direct decomposition of

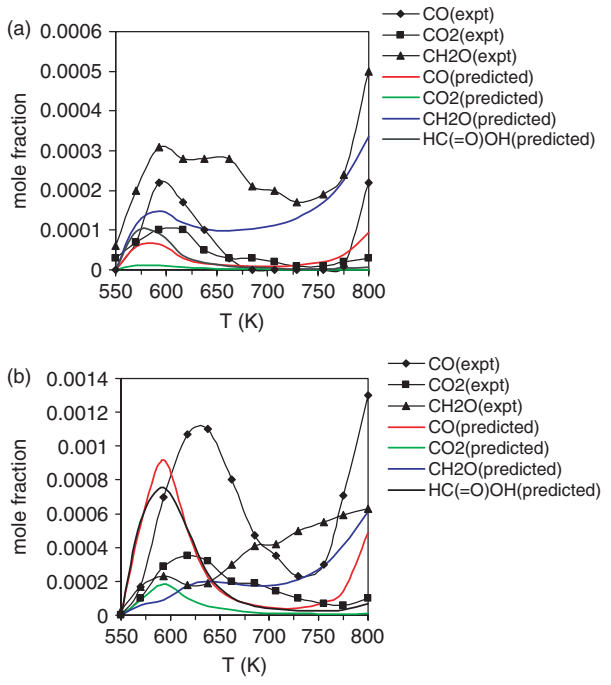

Figure 11. Perfectly stirred reactor predicted product yields. (a) Stoichiometric fuel–oxygen ratio ($\phi = 1.0$). (b) Lean fuel (excess oxygen) ($\phi = 0.2$). Qualitatively, the product trends seem to agree with the experimental product yields of Dagaut *et al.* [36] and the modeling efforts of Curran *et al.* [5]. Quantitative agreement will require more refinement of the underlying mechanism.

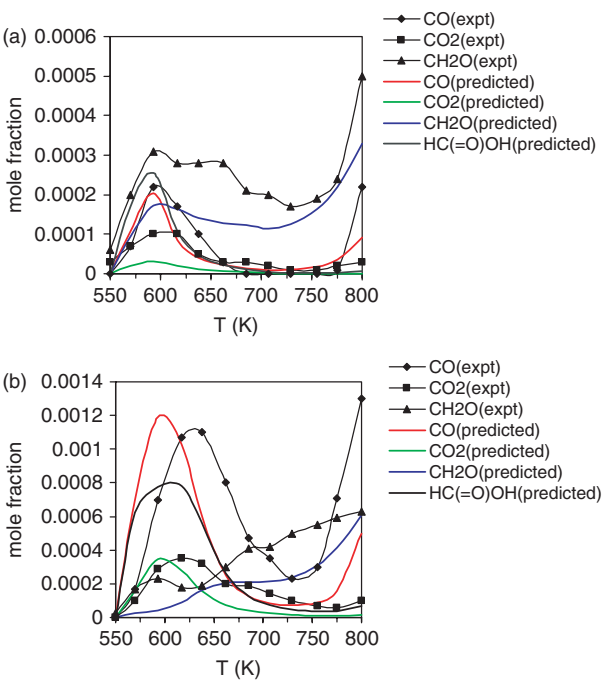

Figure 12. Perfectly stirred reactor predicted product yields. (a) Stoichiometric fuel–oxygen ratio ($\phi = 1.0$). (b) Lean fuel (excess oxygen) ($\phi = 0.2$). The barrier to reaction for reaction (8) has been raised another 1.0 kcal mol^{-1} on top of the 6.0 kcal mol^{-1} used to generate the results in Figure 11. The CO, CO_2, and CH_2=O products of chain-branching are increased quite a bit from the results in Figure 11, suggesting that chain branching is extremely sensitive to reactions involving the $\cdot CH_2OCH_2OOH$ precursor.

$\cdot OCH_2OC(=O)H$ to $H\dot{C}O$ + HC(=O)OH, direct decomposition of HPMF to CH_2OO + HC(=O)OH, and favourable H_2C=O-catalysed rearrangement of CH_2OO to HC(=O)OH).

To increase the yield of the branching products (CO, CO_2, and H_2C=O) in our modeling efforts, we increased the barrier to reaction (8) by another 1.0 kcal mol^{-1} (on top of 6.0 kcal mol^{-1} over the original DFT-B3LYP barrier height). These results are presented in Figures 12(a) and (b). With only a slight increase of 1.0 kcal mol^{-1}, we see a dramatic increase in the CO, CO_2, and H_2C=O yield. We especially see in Figure 12(a) (for the $\phi = 1.0$ case) that CO surpasses the yield of H_2C=O. With a lower rate constant for reaction (8) than the one we used, Curran *et al.*'s [5] modeling efforts also show an overabundance of CO that surpasses the H_2C=O yield. Again, the peak in the 550–700 K yields in the $\phi = 0.2$ case is shifted to the left of the experimental peak (see Figure 12(b)). It is evident from our modeling efforts that more work must still be done to refine the low-temperature DME chain-branching mechanism.

4. Summary and conclusions

First-principles (DFT-B3LYP) rate constants for individual elementary reactions thought to be responsible for dimethyl ether's low-temperature autoignition were estimated. Along the chain propagation pathway (see Figure 1), we have attempted to calculate accurate variational transition state theory rate expressions for reaction (6). The heat of reaction of reaction (6) was adjusted to the heat of reaction implied by Curran *et al.*'s [4,5] heats of formation for $CH_3O\dot{C}H_2$ and $CH_3OCH_2OO\cdot$ to compensate for DFT-B3LYP's lack of multi-reference behaviour and therefore its difficulty in describing O_2 and ROO·. Our predicted VRRKM rate constants were shown to be higher than that of experiment (see Figure 2). Thus, there is a need to more accurately describe the potential surface of reaction (6).

Continuing along the potential chain propagation path, we show that the rate expression through reaction (7) is in better agreement with that of Curran *et al.* [4,5] than with that of Yamada *et al* [10]. The rate expression

used for reaction (7) in the former study by Curran *et al.* may be a more reliable gauge to compare our calculated rate expression for reaction (7) because Yamada *et al.* [10] calculated a very low barrier for reaction (7) compared to the barrier we calculated with DFT-B3LYP (which is more likely to underestimate barriers compared to the CBS-q//MP2 method used by Yamada *et al.*). In previous work [2], we found a transition state to reaction (8) that is much lower in energy compared with the CBS-q calculations of Yamada *et al.* [10] and the estimation made by Curran *et al.* [4,5]. We have shown here that our calculated (using the previous [2] DFT-B3LYP information) rate coefficient for reaction (8) is quite a bit higher than the rate coefficients of Yamada *et al.* [10] and Curran *et al.* [4,5]. We have also found that the rate coefficient through reaction (8) is very pressure sensitive with increasing temperature (see Figure 4). Therefore, we used finite pressure (10 atm) phenomenological rates in our perfectly stirred reactor modeling efforts.

Furthermore, master equation simulations were performed to model the chemical activation phenomenon of the chain propagation mechanism as reported by Sehested *et al.* [6]. We were able to reproduce the qualitative behaviour of the chemical activation, in which chemically (vibrationally) activated $CH_3OCH_2OO\cdot$ reacted to eventually form $2H_2C=O+\cdot OH$ at low pressures (well below atmospheric pressure) and was collisionally stabilised at higher pressures. Though we could not model the 'self-reaction' leading to $CH_3OC(=O)H$ (methyl formate) and CH_3OCH_2OOH reported by Sehested *et al.* [6], the stabilisation of $CH_3OCH_2OO\cdot$ with increasing pressure suggests an increase in self-reaction products. These simulations suggest that the barrier to $\cdot CH_2OCH_2OOH$ dissociation through reaction (8) may be too low. Better agreement with experiment is seen with a $6.0\,kcal\,mol^{-1}$ increase in the barrier to $\cdot CH_2OCH_2OOH$ decomposition. Raising the barrier for reaction (7) by $3.0\,kcal\,mol^{-1}$ produces similar results, but the raising of the barrier for reaction (8) is more likely since some $\cdot CH_2OCH_2OOH$ must stabilise at 1 atm (760 Torr) in order for Liu *et al.* [8] to have observed the branching product, HC(=O)OH, in their flow-reactor experiments.

Along the chain branching pathway (see Figure 1), we have calculated the rate coefficient (using VRRKM) for the addition of O_2 to $\cdot CH_2OCH_2OOH$ (Equation (12)), which has similar trends to that for the addition of O_2 to $CH_3\dot{O}CH_2$ (Equation (6)). Like reaction (6), the heat of reaction for reaction (12) was adjusted to reflect the heat of formation of $\cdot CH_2OCH_2OOH$ and $\cdot OOCH_2OCH_2OOH$. Again, the reason for the underestimation of the heat of formation for reaction (12) by DFT-B3LYP is due to DFT-B3LYP's lack of multi-reference behaviour. Our predicted rate constant (with the aforementioned adjustment to the heat of formation) is greater than that estimated by Curran *et al.* [4,5]. Further along the chain branching path, our predicted rate constant for the isomerisation of $\cdot OOCH_2OCH_2OOH$ to $HOOCH_2O\dot{C}HOOH$ (Equation (13)) is higher than that estimated by Curran *et al.*, [4,5] despite our activation barrier calculated with DFT-B3LYP [4] being higher than that of Curran *et al.*

In our previous energetics work [3], we showed that hydroperoxymethyl formate ($HOOCH_2OC(=O)H$; HPMF) produced in the course of chain branching has multiple unimolecular decomposition pathways. According to our previous energetics results, the four lowest-energy paths to HPMF decomposition are those involving (in order of increasing barrier to reaction) reactions (23), (16), (22), and (15). The comprehensive DME combustion mechanism of Curran *et al.* [4,5] defines reaction (16) as the dominant reaction for HPMF decomposition. However, both the energetics discussed previously [3] and the kinetics analysis conducted here favour the dissociation of HPMF to $HC(=O)OH\cdots CH_2OO$ (reaction (23)) over the dissociation of HPMF via O–O scission (reaction (16)). For complete decomposition of the $HC(=O)OH\cdots CH_2OO$ complex to separate HC(=O)OH and CH_2OO fragments, $\sim 14\,kcal\,mol^{-1}$ is needed, and therefore the endothermicity of both reactions (22) and (16) are roughly equal. This means that reactions (22) (through the $HC(=O)OH\cdots CH_2OO$ complex) and (22) are very competitive. Our VRRKM calculated rate expression is in good agreement with the rate expression estimated by Curran *et al.* [4,5]. However, the $HC(=O)OH\cdots CH_2OO$ complex, which is also expected to undergo 'barrierless' dissociation, involves a 'multi-faceted' bonding of the two fragments that cannot be described with the variational transition state theory approach available to us at this time. Thus the competitiveness of reactions (22) (via the $HC(=O)OH\cdots CH_2OO$ complex) and (16) is rough and will be a subject for further study.

Since we have shown that reaction (22) (via the $HC(=O)OH\cdots CH_2OO$ complex) is competitive with reaction (16), the inclusion of CH_2OO unimolecular and bimolecular reactions was appropriate. CH_2OO reactions are well-known in the realm of atmospheric chemistry. However, CH_2OO reactions have not been

considered before in connection with dimethyl ether/diesel combustion, and rate constants for possible CH_2OO unimolecular and bimolecular reactions are not available for the 298–1000 K temperature range (let alone room temperature). Thus CH_2OO unimolecular and selected bimolecular reaction rate constants were calculated from DFT-B3LYP energies, frequencies, and moments of inertia calculated in this work. Unimolecular reaction of CH_2OO is more likely (both energetically and kinetically) to involve rearrangement of CH_2OO to form dioxirane (reaction (29)) than O–O scission in dioxirane to form methylenebis(oxy) (reaction (30)). The methylenebis(oxy) can undergo further reaction through two paths that are almost equally energetically (reactions (32) and (31)). However, the unimolecular rate expressions for reactions (32) (the decomposition of methylenebis(oxy) to form CO_2 and H_2) and (31) (the decomposition of methylenebis(oxy) to form formic acid) indicate that reaction (32) is slightly more favourable at 600 K (close to peak production of chain branching reactions) than reaction (31).

Global modeling of the combustion of DME at low temperatures was done using perfectly stirred reactor (PSR) simulations. We used the phenomenological elementary rate expressions (10 atm) calculated in this work along with our calculated (with adjustments for consistency with Curran *et al.* [4,5]) and known experimental thermochemical parameters describing heat capacity, enthalpy, and entropy for each species considered in this work. We find that the yields of major low-temperature branching products (CO, CO_2, $H_2C{=}O$, and HC(=O)OH) are most sensitive to reactions (8) (decomposition of $\cdot CH_2OCH_2OOH$ to form two $H_2C{=}O$ and ·OH) and (12) (addition of O_2 to $\cdot CH_2OCH_2OOH$). Reactions (22) (via $CH_2OO\cdots HC(=O)OH$) and (16) are competitive with each other. We have found a route for $\cdot OCH_2OC(=O)H$ decomposition that leads directly to the production of HC(=O)OH and $H\dot{C}O$ (reaction (17)), which has a lower barrier to decomposition than the path proposed by Curran *et al.* through reactions (17) and either (19) or (18) and finally (20) (for the production of HC(=O)OH). Since reaction (21) circumvents the possibility of reaction (19) occurring, CO_2 is not created if reaction (16) is the primary means of HPMF decomposition in the 550–700 K temperature range. However, CO_2 is a major product seen in the experiments of Dagaut *et al.* [36] in the 550–700 K range. Thus reaction (22) (via $CH_2OO\cdots HC(=O)OH$) must be in competition with reaction (16), which produces CH_2OO diradicals that preferentially (according to our unimolecular reaction analysis) decompose to CO_2 and H_2 in the 550–700 K range via reaction (32). Moreover, we find that the yields of major stable products of low-temperature DME combustion in our PSR simulations are not sensitive to the HPMF and CH_2OO bimolecular reactions considered here (Table 5), save for the $H_2C{=}O$-catalysed conversion of CH_2OO to HC(=O)OH, which allows for higher predicted HC(=O)OH yields than seen by Curran *et al.* [5]. Overall PSR results are in qualitative agreement with the experimental results of Dagaut *et al.* [36], having the feature of the major branching products CO, CO_2, and $H_2C{=}O$ peaking in the 550–700 K range where low-temperature chain branching is thought to occur. Further work on low-temperature DME combustion is needed to attain more quantitative agreement with experiment.

Finally, we would like to add here some general ramifications of our work presented here on DME's use in diesel engines. DME combustion within a diesel engine has been reported to have peak pressures and rates of pressure rise in the combustion chamber that are less than the maximum pressures and pressure rise rates of conventional diesel fuel combustion [96]. Therefore, the engine noise created by DME combustion is less than that created by conventional diesel fuel combustion, which is beneficial for the reduction of vibrational damage to the engine [96]. Moreover, the smooth combustion results in high mechanical and thermal efficiency [96]. We speculate that the competition between reaction (16) (decomposition of HPMF via O–O scission), which aids in chain branching by providing the second ·OH radical, and reaction (22) (decomposition of HPMF to HC(=O)OH and CH_2OO via $CH_2OO\cdots HC(=O)OH$), which is unlikely to produce a second ·OH, may possibly subdue the 'explosiveness' of DME's autoignition. Since not all of the HPMF created in the course of the chain branching mechanism are successfully decomposed to $\cdot OH + \text{products}$, the branching rate would be slower compared to the branching rate if all the HPMF were converted to $\cdot OH + \text{products}$. Indeed, there may exist a balance between $CH_2OO + HC(=O)OH$ and $\cdot OH + \cdot OCH_2OC(=O)H$ production that partly explains the favourable low mechanical and combustion noise. Comparison with conventional diesel fuel autoignition mechanistic details would be helpful in determining if this is indeed the case.

5. Supplemental material

1, 10, and 40 atm modified Arrhenius rate expression and DFT-B3LYP energies, optimised geometries and frequencies for reactant, intermediate, transition state, and product species other than those calculated

previously [2,3] can be obtained upon request from the corresponding author.

Acknowledgements

This paper is meant to honor the many contributions of Prof. Raphael Levine to our community's understanding of molecular dynamics. Raphy's discussions with us were crucial at an early stage of our work in the combustion dynamics area; we are extremely grateful to him for those discussions and for his support and advice over the years. A.A. and E.A.C. would also like to thank Drs. S.H. Robertson, E.W. Kaiser, Profs. W.F. Schneider, S.Y. Umanskii and J.R. Barker, and Mr. M.W. Stoker and J.J. Szente for their helpful suggestions. Funding for this work was provided by the Ford Motor Company.

References

[1] S.S. Sorenson, Trans. ASME **123**, 652, and references therein (2001).
[2] A. Andersen and E.A. Carter, Isr. J. Chem. **42**, 245 (2002).
[3] A. Andersen and E.A. Carter, J. Phys. Chem. A **107**, 9463 (2003).
[4] S.L. Fischer, F.L. Dryer, and H.J. Curran, Int. J. Chem. Kinet. **32**, 713 (2000).
[5] H.J. Curran, S.L. Fischer, and F.L. Dryer, Int. J. Chem. Kinet. **32**, 741 (2000).
[6] J. Sehested, T. Møgelberg, T.J. Wallington, *et al.*, J. Phys. Chem. **100**, 17218 (1996).
[7] J. Sehested, K. Sehested, J. Platz, *et al.*, Int. J. Chem. Kinet. **29**, 627 (1997).
[8] I. Liu, N.W. Cant, J.H. Bromly, *et al.*, Chemosphere **42**, 583 (2001).
[9] H.J. Curran, W.J. Pitz, C.K. Westbrook, *et al.*, Int. J. Chem. Kinet. **30**, 229 (1998).
[10] T. Yamada, J.W. Bozzelli, and T.H. Lay, Int. J. Chem. Kinet. **32**, 435 (2000).
[11] P.J. Stephens, F.J. Devlin, C.F. Chabalowski, *et al.*, J. Phys. Chem. **98**, 11623 (1994).
[12] R. Krishnan, J.S. Binkley, R. Seeger, *et al.*, J. Chem. Phys. **72**, 650 (1980).
[13] J.C. Rienstra-Kiracofe, W.D. Allen, and H.F. Schaefer III, Phys. Chem. A **104**, 9823 (2000).
[14] M. Olzmann, E. Kraka, D. Cremer, *et al.*, J. Phys. Chem. A **101**, 9421 (1997).
[15] D. Cremer, E. Kraka, and P.G. Szalay, Chem. Phys. Lett. **292**, 97 (1998).
[16] P. Aplincourt and M.F. Ruiz-López, J. Am. Chem. Soc. **122**, 8990 (2000).
[17] G.A. Petersson, D.K. Malick, W.G. Wilson, *et al.*, J. Chem. Phys. **109**, 10570 (1998).
[18] F. Jensen, *Introduction to Computational Chemistry* (Wiley, Chichester, West Sussex, UK, 1999).
[19] K.P. Novoselov, D.B. Shirabaikin, S.Y. Umanskii, *et al.*, J. Comput. Chem. **23**, 1375 (2002).
[20] KHIMERA v3.1, © Motorola Inc., 2001.
[21] W. Forst, *Theory of Unimolecular Reactions* (Academic Press, New York, 1993).
[22] R.G. Gilbert and S.C. Smith, *Theory of Unimolecular and Recombination Reactions* (Blackwell Scientific, Oxford, 1990).
[23] K.A. Holbrook, M.J. Pilling, and S.H. Robertson, *Unimolecular Reactions*, 2nd ed. (Wiley, Chichester, West Sussex, UK, 1996).
[24] M.J. Pilling and S.H. Robertson, A. Rev. Phys. Chem. **54**, 245 (2003).
[25] R.J. Kee, F.M. Rupley, J.A. Miller, *et al.*, *CHEMKIN Collection, Release 3.7.1* (San Diego, CA, USA, 2003), Reaction Design, Inc.
[26] S.J. Klippenstein, A.F. Wagner, R.C. Dunbar, *et al.*, *VARIFLEX* Version 1.00, July 16 1999.
[27] R.C. Reid, J.M. Prausnitz, and B.E. Poling, *The Properties of Gases & Liquids* (McGraw-Hill, Boston, MA, 1987).
[28] ChemDraw Ultra 6.0, © 1985–2000 CambridgeSoft Corporation. All rights reserved.
[29] Y.P. Varshni, Rev. Mod. Phys. **29**, 664 (1957).
[30] S.J. Klippenstein, L.R. Khundkar, A.H. Zewail, *et al.*, J. Chem. Phys. **89**, 4761 (1988).
[31] Barker J.R., MultiWell-1.3.3 software, 2003.
[32] J.R. Barker, Int. J. Chem. Kinet. **33**, 232 (2001).
[33] B.M. Toselli, M. Brenner, W.E. Chin, *et al.*, J. Chem. Phys. **95**, 176 (1991).
[34] McBride B.J. Gordon S., NASA Report 1967, NASA TN-4097 (http://cea.grc.nasa.gov).
[35] P. Dagaut, J.-C. Boettner, and M. Cathonnet, in *26th Symposium (International) on Combustion* (The Combustion Institute, Pittsburgh, 1996), p. 627.
[36] P. Dagaut, C. Daly, J.M. Simmie, *et al.*, in *27th Symposium (International) on Combustion* (The Combustion Institute, Pittsburgh, PA, 1998).
[37] K. Hoyermann and F. Nacke, *26th Symposium (International) on Combustion* (The Combustion Institute, Pittsburgh, 1996).
[38] M.E. Jenkin, G.D. Hayman, T.J. Wallington, *et al.*, J. Phys. Chem. **97**, 11723 (1993).
[39] M.M. Maricq, J.J. Szente, and J.D. Hybl, J. Phys. Chem. A **101**, 5155 (1997).
[40] F. Su, J.G. Calvert, and J.H. Shaw, J. Phys. Chem. **84**, 239 (1980).
[41] H. Niki, P.D. Maker, C.M. Savage, *et al.*, J. Phys. Chem. **85**, 1024 (1981).
[42] C.S. Kan, F. Su, J.G. Calvert, *et al.*, J. Phys. Chem. **85**, 2359 (1981).
[43] R. Gutbrod, E. Kraka, R.N. Schindler, *et al.*, Am. Chem. Soc. **119**, 7330 (1997).
[44] R. Gutbrod, S. Meyer, M.M. Rahman, *et al.*, Int. J. Chem. Kinet. **29**, 717 (1997).
[45] R. Atkinson, S.M. Aschmann, J. Arey, *et al.*, J. Geophys. Res. **97**, 6065 (1992).

[46] S. Hatakeyama, H. Kobayashi, and H. Akimoto, J. Phys. Chem. **88**, 4736 (1984).
[47] N.M. Donahue, J.H. Kroll, J.G. Anderson, *et al.*, Geophys. Res. Lett. **25**, 59 (1997).
[48] R. Atkinson, J. Chem. Phys. Ref. Data **26**, 215 (1997).
[49] J. Thamm, S. Wolff, M.V. Turner, *et al.*, Chem. Phys. Lett. **258**, 155 (1996).
[50] R.I. Martinez and J.T. Herron, J. Envir. Schi. Hlth. A **16**, 623 (1981).
[51] S. Hatakeyama, H. Bandow, M. Okuda, *et al.*, J. Phys. Chem. **85**, 2249 (1981).
[52] P. Neeb, O. Horie, and G.K. Moortgat, Int. J. Chem. Kinet. **28**, 721 (1996).
[53] P. Neeb, F. Sauer, O. Horic, *et al.*, Atmos. Environ. **31**, 1417 (1997).
[54] S. Wolff, A. Boddenberg, J. Thamm, *et al.*, Atmos. Environ. **31**, 2965 (1997).
[55] R. Atkinson, D.I. Baulch, R.A. Cox, *et al.*, J. Phys. Chem. Ref. Data **21**, 1125 (1992).
[56] S.W. Benson, *Thermochemical Kinetics*, 2nd ed. (Wiley, New York, 1976), p. 300.
[57] E.R. Ritter and J.W. Bozzelli, Int. J. Chem. Kinet. **23**, 767 (1991).
[58] T. Lay, J.W. Bozzelli, A.M. Dean, *et al.*, J. Phys. Chem. **99**, 14514 (1995).
[59] A. Andersen and E.A. Carter, J. Phys. Chem. A **106**, 9672 (2002).
[60] J.A. Miller, S.J. Klippenstein, and S.H. Robertson, in *Proceedings of the Combustion Institute 2000* (The Combustion Institute, Pittsburgh, 2000).
[61] J.A. Miller and S.J. Klippenstein, J. Phys. Chem. A **104**, 2061 (2000).
[62] A.F. Wagner, I.R. Slagle, D. Sarzynski, *et al.*, J. Phys. Chem. **94**, 1853 (1990).
[63] R.P. Ruiz and K.D. Bayes, J. Phys. Chem. **88**, 2592 (1984).
[64] P.Y. Ayala and H.B. Schlegel, J. Chem. Phys. **108**, 2314 (1998).
[65] L.F. Loucks and K.J. Laidler, Can. J. Chem. **45**, 2767 (1967).
[66] Andersen A., Carter E.A., J. Phys. Chem. A, **110**, 1393 (2001).
[67] K.A. Sahetchian, R. Rigny, J. Tardieu de Maleissye, *et al.*, in *24th Symposium (International) on Combustion* **24**, 637 (1992).
[68] Y. Georgievskii and S.J. Klippenstein, J. Phys. Chem. A **107**, 9776 (2003).
[69] P. Aplincourt and M.F. Ruiz-López, J. Phys. Chem. A **104**, 380 (2000).
[70] J.T. Herron and R.E. Huie, J. Am. Chem. Soc. **99**, 5430 (1977).
[71] J.T. Herron and R.E. Huie, Int. J. Chem. Kinet. **10**, 1019 (1978).
[72] D. Gremer, J. Gauss, E. Kraka, *et al.*, Chem. Phys. Lett. **209**, 547 (1993).
[73] J.M. Anglada, J. Bofill, S. Olivella, *et al.*, J. Am. Chem. Soc. **118**, 4636 (1996).
[74] R. Gutbrod, R.N. Shindler, E. Kraka, *et al.*, Chem. Phys. Lett. **96**, 221 (1996).
[75] J.M. Anglada and J.M. Bofill, J. Org. Chem. **62**, 2720 (1997).
[76] J.M Andalga, J.M. Bofill, S. Olivella, *et al.*, Phys. Chem. **102**, 3398 (1998).
[77] D. Cremer, T. Schidt, J. Gauss, *et al.*, Angew. Chem. Int. Ed. Engl. **27**, 427 (1988).
[78] J. Gauss and D. Cremer, Chem. Phys. Lett. **133**, 420 (1987).
[79] R.D. Bach, J.L. André, A.L. Owensby, *et al.*, J. Am. Chem. Soc. **114**, 7207 (1992).
[80] G. Karlström and B.O. Roos, Chem. Phys. Lett. **79**, 416 (1981).
[81] J.H. Kroll, S.R. Sahay, J.G. Anderson, *et al.*, J. Phys. Chem. A **105**, 4446 (2001).
[82] P. Neeb, O. Horie, and G.K. Moortgat, Chem. Phys. Lett. **246**, 150 (1995).
[83] S. Hatakeyama, H. Kobayashi, Z. Lin, *et al.*, J. Phys. Chem. **90**, 4131 (1986).
[84] R. Atkinson and A.C. Lloyd, J. Phys. Chem. Ref. Data **13**, 315 (1984).
[85] R. Crehuet, J.M. Anglada, and J.M. Bofill, Chem. Eur. J. **7**, 2227 (2001).
[86] J.M. Anglada, P. Aplincourt, J.M. Bofill, *et al.*, Chem Phys Chem **3**, 215 (2002).
[87] A.S. Hasson, M.Y. Chung, K.T. Kuwata, *et al.*, J. Phys. Chem. A **107**, 6176 (2003).
[88] H.E. O'Neal and C. Blumstein, Int. J. Chem. Kinet. **5**, 397 (1973).
[89] W.R. Wadt and W.A. Goddard III, J. Am. Chem. Soc. **97**, 3004 (1975).
[90] L.B. Harding and W.A. Goddard III, J. Am. Chem. Soc. **100**, 7180 (1978).
[91] NIST Standard Reference Database 69, March 2003 Release: NIST Chemistry WebBook.
[92] M.W. Chase, Jr., J. Phys. Chem. Ref. Data **9**, 1 (1998).
[93] J.P. Guthrie, J. Am. Chem. Soc. **96**, 3608 (1974).
[94] S.E. Stein and R.L. Brown, in *NIST Standard Reference Database Number 69 NIST Chemistry WebBook* edited by P.J. Linstrom and W.G. Mallard (National Institute of Standards and Technology, Gaithersburg, MD, 2003) (http://webbook.nist.gov).
[95] R.D. Suenram and F.J. Lovas, J. Am. Chem. Soc. **100**, 5117 (1978).
[96] Z.H. Huang, H.W. Wang, H.Y. Chen, *et al.*, Proc. Inst. Mech. Engrs **213**, 647 (1999).
[97] J.B. Pedley, R.D. Naylor, and S.P. Kirby, *Thermochemical Data of Organic Compounds* (Chapman and Hall, New York, 1986).